ADVANCED ENERGY MATERIALS
www.advenergymat.de

Boon and Bane of Local Solid State Chemistry on the Performance of LSM-Based Solid Oxide Electrolysis Cells

Hanna Türk, Xuan Quy Tran,* Patricia König, Adnan Hammud, Vaibhav Vibhu, Franz-Philipp Schmidt, Dirk Berger, Sören Selve, Vladimir Roddatis, Daniel Abou-Ras, Frank Girgsdies, Yu-Te Chan, Thomas Götsch, Hebatallah Ali, Izaak C. Vinke, L.G.J (Bert) de Haart, Michael Lehmann, Axel Knop-Gericke, Karsten Reuter, Rüdiger-A. Eichel, Christoph Scheurer, and Thomas Lunkenbein**

High-temperature solid oxide cells are highly efficient energy converters. However, their lifetime is limited by rapid deactivation. Little is known about the local, atomic scale transformation that drive this degradation. Here, reaction-induced changes are unraveled at the atomic scale of a solid oxide electrolysis cell (SOEC) operated for 550 h by combining high-resolution scanning transmission electron microscopy with first-principles and force-field-based atomistic simulations. We focus on the structural evolution of lanthanum strontium manganite (LSM)/yttria-stabilized zirconia (YSZ) regions and the corresponding solid–solid interface. It is found that the strong inter-diffusion of cations leads to the additional formation and growth of a multitude of localized structures such as a solid solution of La/Mn, nano-domains of secondary structures or antisite defects in the YSZ, as well as a mixed ion and electron conduction region in the LSM and complexion. These local structures can be likewise beneficial or detrimental to the performance, by either increasing the catalytically active area or by limiting the supply of reactants. The work provides unprecedented atomistic insights into the influence of local solid-state chemistry on the functioning of SOECs and deepens the understanding of the degradation mechanism in SOECs, paving the way towards nanoscopic rational interface design for more efficient and durable cells.

1. Introduction

The genesis of the interfacial structure under reaction conditions often governs the performance and aging of a functional solid. As opposed to gas- or liquid-phase catalysis, the determining interface in solid oxide cells (SOCs) is hidden between two solids, and its structural evolution at high temperatures is dominated by slow and diffusional solid-state processes. Stabilization by the surrounding bulk structure also allows the build-up of novel transient and metastable phases, which are often referred to as complexions and may not exist at other interfaces or as a pure bulk phase.[1,2] Details of the structure and chemistry at these solid-solid interfaces can thus not straightforwardly be extrapolated from known bulk properties, but are at the same time of paramount importance for the functioning of solid oxide fuel and electrolysis cells (SOFCs, SOECs).[3,4]

H. Türk, X. Q. Tran, P. König, A. Hammud, F.-P. Schmidt, F. Girgsdies, Y.-T. Chan, T. Götsch, H. Ali, A. Knop-Gericke, K. Reuter, C. Scheurer, T. Lunkenbein
Fritz-Haber-Institut der Max-Planck-Gesellschaft, Faradayweg 4–6
14195 Berlin, Germany
E-mail: hanna.tuerk@epfl.ch; xqtran@fhi-berlin.mpg.de; lunkenbein@fhi-berlin.mpg.de

H. Türk
Laboratory of Computational Science and Modeling, IMX
École Polytechnique Fédérale de Lausanne
Lausanne 1015, Switzerland

The ORCID identification number(s) for the author(s) of this article can be found under https://doi.org/10.1002/aenm.202405599

DOI: 10.1002/aenm.202405599

V. Vibhu, H. Ali, I. C. Vinke, L. (Bert) de Haart, R.-A. Eichel
Institute of Energy Technologies, Fundamental Electrochemistry (IET-1)
Forschungszentrum Jülich GmbH
52425 Jülich, Germany

D. Berger, S. Selve
Technische Universität Berlin
Center for Electron Microscopy
Straße des 17. Juni 135, 10623 Berlin, Germany

V. Roddatis
GFZ German Research Centre for Geosciences
Telegrafenberg, 14473 Potsdam, Germany

D. Abou-Ras
Department Structure and Dynamics of Energy Materials
Helmholtz-Zentrum Berlin für Materialien und Energie GmbH
Hahn-Meitner-Platz 1, 14109 Berlin, Germany

M. Lehmann
Technische Universität Berlin
Institute of Optics and Atomic Physics
Straße des 17. Juni 135, 10623 Berlin, Germany

These systems, usually composed of earth-abundant elements,[5] convert renewably generated electricity into chemical fuels and back. At temperatures above 600 °C, SOC-based energy conversion systems can reach an outstanding energy efficiency of up to 80%.[6]

Although they seemingly meet the prerequisites for flexible and long-term storage systems in a modern energy infrastructure,[5,6] they suffer from rapid degradation at the air electrode (anode) during electrolysis.[7,8] The causes of degradation have been related to a multi-scale phenomenon[9,10] including delamination and pore formation at the electrode/elecrolyte interfaces,[11,12] an increase of ohmic resistance,[13] segregation of cations and the formation of Mn-rich oxide precipitates or pyrochlore structures.[14–21] These oxides affect detrimentally the electrical[19] and ionic conductivities,[22] and exhibit different thermal expansions compared to the parent oxides,[19] which can worsen the delamination effect at electrode/electrolyte interfaces.[23]

Figure 1a illustrates the assembly of a typical cell and its functionality in electrolysis mode. It consists of the ceramic electrolyte yttria-stabilized zirconia (YSZ, $(Y_2O_3)_x(ZrO_2)_{1-x}$), which is characterized by its fast oxygen-ion conductivity, and a porous composite between YSZ with either metallic Ni (cathode) or strontium-doped lanthanum manganite perovskite (LSM, $(La,Sr)MnO_{3-\delta}$, anode), which is a pure electron conductor. This combination of materials at the anode side offers the possibility of investigating atomistic processes when the solid electrolyte comes into direct contact with the electrode without being separated by a protective layer. A protective layer would be, for instance, necessary for mixed ion-electron conductive (MIEC) anodes. The importance of LSM-based electrodes for high-temperature electrolysis has recently been highlighted.[24–28] The structure of such a ceramic/metal mixture (termed cermet) of a typical anode is shown in Figure 1b. The triple-phase boundaries (TPBs), where the LSM, YSZ and gas phase come into contact, are the chemically active regions as schematically depicted in Figure 1c,d.

For developing rational large-scale design concepts that focus on lifetime enhancement and integration into the energy system, an atomic-scale understanding similar to Figure 1e is mandatory. This understanding involves the evolution of the interfacial structures under thermal electrochemical biasing including the spatial identification of nucleation centers of transient structures and their structural integrity within the oxide phases and how they relate to the performance of the device.

Although this has in part been tackled in previous studies, a direct experimental evidence of the existence of those structures remains scarce or is discussed controversially. For instance, Chen et al. reported nano-sized precipitates and amorphous voids at the LSM/YSZ interface after operation in humidified air,[16] while He et al. described a semi-coherent interface without any hints of an amorphous phase.[29,30] Backhaus–Ricoult et al. revealed a crystalline interface and a solid solution of Mn^{2+} on the YSZ side of the interface.[31,32] Most recently, the concept of a nano-scale complexion[33,34] at the LSM/YSZ interface was described, which is characterized by a strong compositional gradient and partial amorphization of the neighboring YSZ structure.[35–37] It is built up by solid-state diffusion from the neighboring bulk oxides and exhibits improved oxygen diffusivity. However, the electrochemical potential and property of the depleted zones in the neighboring bulk oxides as well as the electron conductivity of the complexion has yet not been addressed.

Here, we show that after 550 h at 800 °C under −0.3 A·cm^{-2} diffusional solid state processes lead to the additional formation and growth of an MIEC at the LSM site as well as a solid solution of La/Mn, secondary structures and antisite defects at the YSZ site in interface-near regions. As we will show these structural transformation can be detrimental or beneficial for the performance of the cell. Our conclusions are based on investigating a typical interface between 8YSZ (ZrO_2) doped with 8 mol% (Y_2O_3) electrolyte and LSM20 ($(La_{0.8}Sr_{0.2})_{0.95}MnO_{3-\delta}$) as anode material combining chemical electron microscopy[38] with theoretical modeling. We highlight here that these phenomena occur locally and coexist within the same sample. Their implications on activation and deactivation are discussed. The comprehensive description of local transport processes along and across grain boundaries in functional solids leads to an overall knowledge gain, which expands our understanding of the degradation mechanism of the anode side in SOECs.

2. Results and Discussion

2.1. On the Electrochemical Behavior of SOECs

Figure 2a shows the evolution of the electrochemical performance of the investigated cell for 550 h. In the first 50 h, a rapid rise of the cell voltages was observed. With time on stream, the degradation rate significantly declined indicating that the internal structure of the cell is changed such that the initial fast degradation effect is compensated. This behavior is in line with other nominally identical cells that are part of this study (Figure S3 a, Supporting Information) and additional reports.[39,40] In addition, we found that the complex behavior of the cell voltage is accompanied by changes in the distribution of relaxation times (DRT), which have been calculated from the recorded impedance of the cell before and after 550 h, as illustrated in Figure 2b,c. Major changes of the DRT peaks were observed in the middle frequency (MF) range, most notably is the change observed at MF2~165 Hz, which is accompanied by minor contributions from MF1~55 Hz and MF3~400 Hz and in line with the observations made from a nominally identical cell (Figure S3 c, Supporting Information). The peaks in the high-frequency (HF, >1000 Hz) region, which are generally associated with charge transfer processes are only changing marginally.[41] In order to judge whether these findings are dominated by structural changes at the cathode or anode side, additional experiments have been conducted.

A decay of the O_2 partial pressure on the anode side (Figure S4 a, Supporting Information) results in an increase of the middle-frequency DRT peaks. This behavior can be related to a reduction of the oxygen exchange kinetics on the surface due to Sr surface

A. Knop-Gericke
Max Planck Institute for Chemical Energy Conversion, Department of Heterogeneous Reactions, Stiftstraße 34–36
45470 Mülheim an der Ruhr, Germany
R.-A. Eichel
RWTH Aachen University, Institute of Physical Chemistry, Landoltweg 2
52074 Aachen, Germany

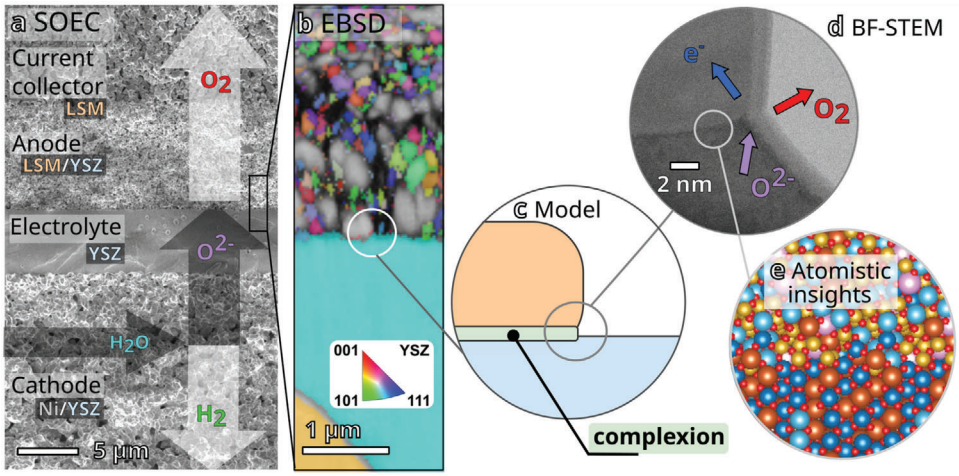

Figure 1. Morphology, structure, and electrochemical operation of a SOEC. a) Scanning electron microscopy image (SEM) of the SOEC components and the corresponding reactions occurring during operation. b) Electron backscatter diffraction (EBSD) map for the interface between the porous LSM + 8YSZ electrode and the 8YSZ electrolyte at the sub-micrometer scale, which shows the random orientation of cubic YSZ grains (space group: *Fm-3m*). Note that the LSM grains with the rhombohedral structure (space group: *R-3c*) only appear in gray color. A more complete overview of the cell with SEM, X-ray Diffraction (XRD) and EBSD characterization is available in Figures S1 and S2 (Supporting Information). c, d) Schematic representation and experimental bright-field scanning transmission electron microscopy (BF- STEM) image, respectively, of a local region containing the LSM/YSZ interface and the triple phase boundary (TPB) site where the oxygen evolution reaction (OER) takes place. e) Atomistic resolution of the LSM/YSZ interface gained from theoretical simulations.

segregation and SrO formation, which is additionally promoted by an oxygen-deficient atmosphere.[42] Sr surface segregation has also been identified in our cells.[36] A change of the N_2 or steam partial pressure on the cathode side generally resulted in DRT responses in the low-frequency range (LFs, ≈4–15 Hz, Figure S4 b,c, Supporting Information). This finding suggests that the anode is predominantly responsible for the observed electrochemical behavior of the entire cell. Nevertheless, a shoulder peak at MF3~400 Hz in Figure 2c might be associated to a minor contribution from the cathode side to the overall cell behavior (compare Figure S4 c, Supporting Information).

In addition, we compare the resistance recorded before and after the aging experiments (corresponding to Figure 2b,c). A slight change in the ohmic resistance (i.e. 0.187 and 0.181 Ω.cm^2, respectively) can be observed while the major contribution stems from an increase in the polarization resistance (i.e. 0.401 and 0.591 Ω.cm^2, respectively), in agreement with other cells (Figure S3 d, Supporting Information). Previous studies[40,43,44] have connected the redistribution of Ni on the cathode side of the SOEC to an increase in the ohmic resistance during continuous operation. Therefore, a relatively stable ohmic resistance as seen in our study suggests only minimal changes in the cathodic Ni/YSZ microstructure at the applied current density of −0.3 A·cm^{-2}. This is further corroborated by a comparative analysis using low-voltage SEM imaging focusing on the Ni-YSZ microstructure of the cathode side (Figure S5, Supporting Information). We find that the Ni-YSZ || YSZ interface remained intact in a cell operated for 550 h, which is in contrast to other studies where a significant loss of Ni percolated networks was clearly visible[40,44,45]). This hypothesis complies with findings by Mogensen et al.[46] The authors concluded that in cells operated at low current densities (up to 0.25 A·cm^{-2}) Ni migration is absent for up to a few thousand hours time on stream. In contrast, pronounced changes on the cathode side of SOECs on shorter time scales are generally expected to happen at current densities between 0.5 and 1.0 A·cm^{-2}.[46]

Hence, our results from the electrochemical characterization of the SOEC cells indicate that under the applied conditions the main contribution to the cell voltage behavior is associated with the anode side of the SOEC. We, therefore, focus on describing the prevailing structures at the anode side of an aged SOEC cell on the atomic scale in order to provide an in-depth structural understanding leading to electrochemical degradation.

2.2. Structural Pluralism at the Anode/Electrolyte Interface

2.2.1. The Formation of Nano-Sized Ordered Domains

The anode of a SOEC operated for 550 h (SOEC #1) has been subjected to electron transparent lamellae preparation by a focused ion beam instrument (FIB) in order to explore the structural pluralism at the atomic scale close to the LSM/YSZ interface by chemical electron microscopy. **Figure 3** shows scanning transmission electron microscopy (STEM) micrographs of different YSZ regions near the LSM/YSZ interface of an operated cell along three different orientations, $[010]_c$, $[011]_c$ and $[111]_c$. Figure 3a,b show $[010]_c$ and $[011]_c$ oriented YSZ grains displaying striking $(200)_c$-type layers which predominantly occur in the vicinity of LSM/YSZ interfaces. This observation is also in line with the additional $\frac{1}{2}(200)$ superspots found in the Fast Fourier transform (FFT), which evinces the existence of a superstructure with distinct long-range order. Furthermore, the inverse FFT (iFFT) images based on these superspots clearly show a discrete network of nano-sized domains, which are distinct from the surrounding cubic YSZ. The ordered layers of the $[010]_c$ viewing

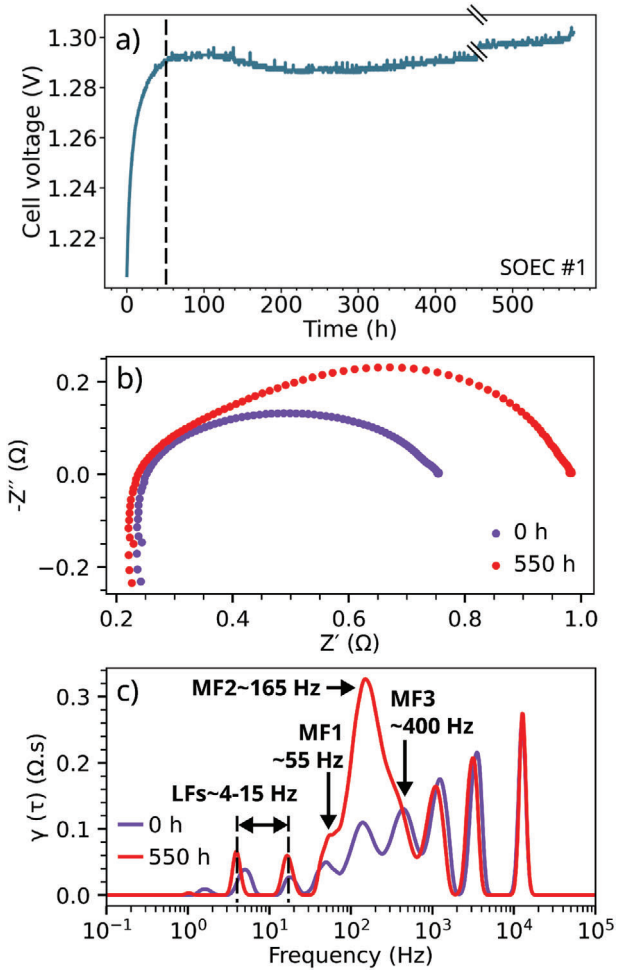

Figure 2. Electrochemical aging of an SOEC operated for 550 h (SOEC #1). a) Temporal evolution of the cell voltage for an SOEC consisting of an Ni/8YSZ substrate and cathode, an 8YSZ electrolyte and an LSM/8YSZ anode. The cell was operated at 800 °C and with an applied current density of −0.3 A·cm^{-2} (9 L h^{-1} H_2:H_2O 50:50 and 9 L h^{-1} air). Around 450 h, a power outage caused an interruption in the measurement, resulting in a small offset of the cell voltage. b) Nyquist plot of the impedance spectra recorded at 800 °C under an open cell voltage (OCV) at the beginning and the end of the aging test shown in (a). c) Distribution of relaxation times (DRT) analysis of the impedance spectra. The lambda value used was 10^{-7}.

direction seem to prefer the $(200)_c$ plane instead of the $(002)_c$ equivalent (Figures 3a), implying a correlation with the direction of the oxygen influx towards the LSM/YSZ interface. Similar features were also observed in Figure 3c showing a viewing direction of $[111]_c$. Note that such ordered structures were hardly observed at similar YSZ electrolyte regions close to the LSM/YSZ interfaces of non-operated cells (Figures S6 and S7, Supporting Information), while they can be present in the small grains (≈200 nm) in the mixed region of the LSM/YSZ anode (Figure S8, Supporting Information) or in the bulk of YSZ (Sections S10 and S11, Supporting Information). Additional images recorded from sample areas near the LSM/YSZ interfaces further corroborate our observation (Figures S7 and S9, Supporting Information). Moreover, reflections that could be assigned to the superstructure have not been observed in X-ray diffraction indicating that the situation described in Figure 3 is a very local phenomenon (Figure S10, Supporting Information).

2.2.2. On the Existence of Tetragonal Inclusions at the LSM/YSZ Interface

Next, we aim to explore the underlying structures of these ordered domains at the atomic scale. Based on the tetragonal structural model[47] (**Figure 4a**), the corresponding simulation of the electron diffraction (ED) pattern along the $[100]_t$ (=$[011]_c$) direction (Figure 4b) provides a good match to the two-fold superstructure reflections found in Figure 3b for the $(002)_t$ (=$(200)_c$) crystal planes. Furthermore, using annular bright-field (ABF)-STEM imaging (Figure 4c) we were able to trace the origin of this superstructure back to the oxygen distribution. In this imaging mode oxygen can be distinguished from the Zr/Y atomic columns. Notably, an uneven intensity distribution arising from the oxygen anions has been observed that are positioned left and right from the Y/Zr cations in both the experimental and simulated images (Figure 4c), which differs from the more symmetrical motif expected for cubic YSZ. This feature is also accompanied by contrast alterations between the neighboring oxygen-containing layers along the y-axis of the image (red arrows in Figure 4c). These effects can be attributed to the tetragonal distortion occurring along the c-axis, resulting in the asymmetrical arrangement of the displaced oxygen atoms with respect to the Y/Zr cations (Figure 4a). In addition, the integration over the image intensity of the LAADF-STEM image, presented in Figure 4d along the horizontal direction, resulted in an average lattice spacing of 2.57 ± 0.04 Å (Figure 4e). This is in good agreement with the referenced value of 2.58 Å for the equally-spaced $d(002)_t$ (=$d(200)_c$) crystal plane obtained from the tetragonal model given in Figure 4a. The formation of the tetragonal YSZ phase close to the LSM/YSZ interface is in agreement with previous reports[16] and also suggests a local depletion of Y.[47] Furthermore, a reduction of the oxygen mobility by a factor of two in the tetragonal YSZ compared to the cubic polymorph is expected.[48]

2.2.3. On the Existence of Pyrochlore-Like Structures at the LSM/YSZ Interface

The superstructure reflections presented in Figure 3a are incompatible with the tetragonal YSZ structure (Figure S12, Supporting Information). Thus, an additional structure apart from the tetragonal YSZ inclusion must exist. To unravel the structure of this ordered phase we first explore the oxygen distribution by ABF-STEM imaging. As shown in **Figure 5a**, the signal for oxygen atoms appears weaker, yet discernible from the Zr/Y atomic columns. This complements the corresponding LAADF-STEM image where only the metal cations are visible (Figure 5b). Interestingly, we find that the oxygen atoms are systematically absent for every second vertical row (red arrows in Figure 5a), which is different from the surrounding YSZ (Figure S14, Supporting Information). This suggests a two-fold layered ordering of oxygen vacancies ($V_o^{\bullet\bullet}$). As a result, an interaction between $V_o^{\bullet\bullet}$ and other cations such as Y in an orderly manner is expected.[49–51]

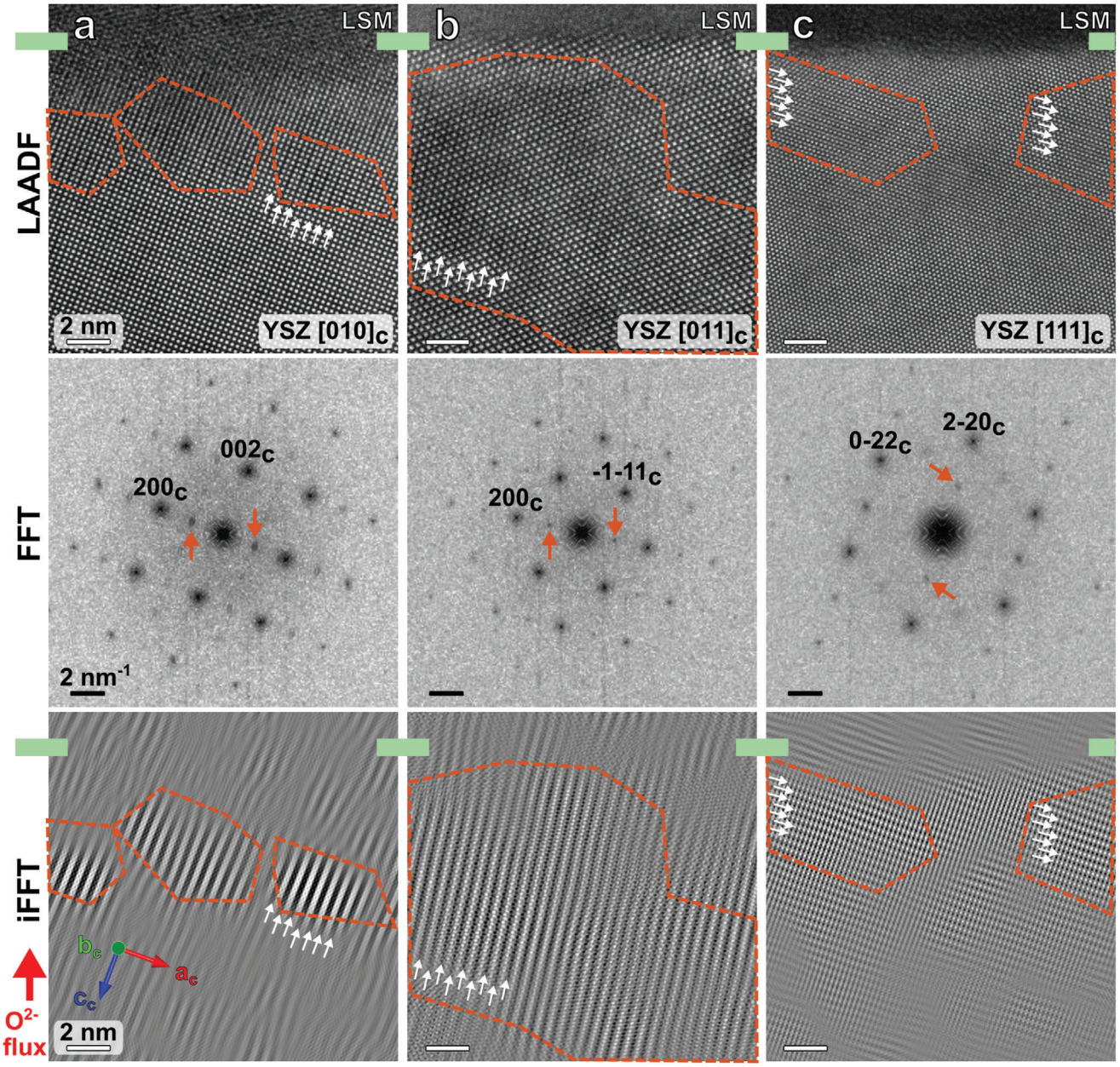

Figure 3. Ordered structure domains near the interfaces between LSM and bulk YSZ electrolyte of the cell operated for 550 h (SOEC #1). a–c) Low angle annular dark-field (LAADF)-STEM, corresponding Fast Fourier transform images (FFT) of the entire LAADF-STEM images, and reconstructed images using the inverse Fast Fourier transform (iFFT) at the LSM/YSZ interfaces along different orientations of the cubic YSZ, that is, $[010]_c$, $[011]_c$ and $[111]_c$, respectively. The striped features can be seen in both imaging modes as highlighted by the white arrows and orange dashed lines, which indicate a network of discrete domains of ordered structures. This is in agreement with the extra superspots in the corresponding FFTs (orange arrows). Note, that the iFFT images are only based on these superspots. The green bars indicate the positions of the LSM/YSZ interfaces. The variation of sample thickness does not influence the FFT patterns discussed above as shown in Figure S11 (Supporting Information).

The real-space projected interatomic distances between neighboring cations was extracted by 2D Gaussian fitting and is denoted as *dx* and *dy* in Figure 5c,d,e (see also Figure S16, Supporting Information). The resulting spatial maps have been superimposed with the corresponding ABF-STEM image for which Figure 5c shows the *dx* distribution and Figure 5d displays the corresponding *dy* map. We find an alternating contraction and expansion of the interatomic distances *dx* in the horizontal direction, which was not observed for the vertical components *dy*. This contraction and expansion of the interatomic distances *dx* is reflected in the bimodal distribution in the upper histogram chart presented in Figure 5e giving rise to distances of 2.39 ± 0.08 and 2.74 ± 0.07 Å, respectively. These expanded layers are correlated with the oxygen-deficient layers (Figure 5a,c, red arrows). The absence of oxygen leads to positively charged vacancies $V_o^{\bullet\bullet}$, whose presence induces Coulomb

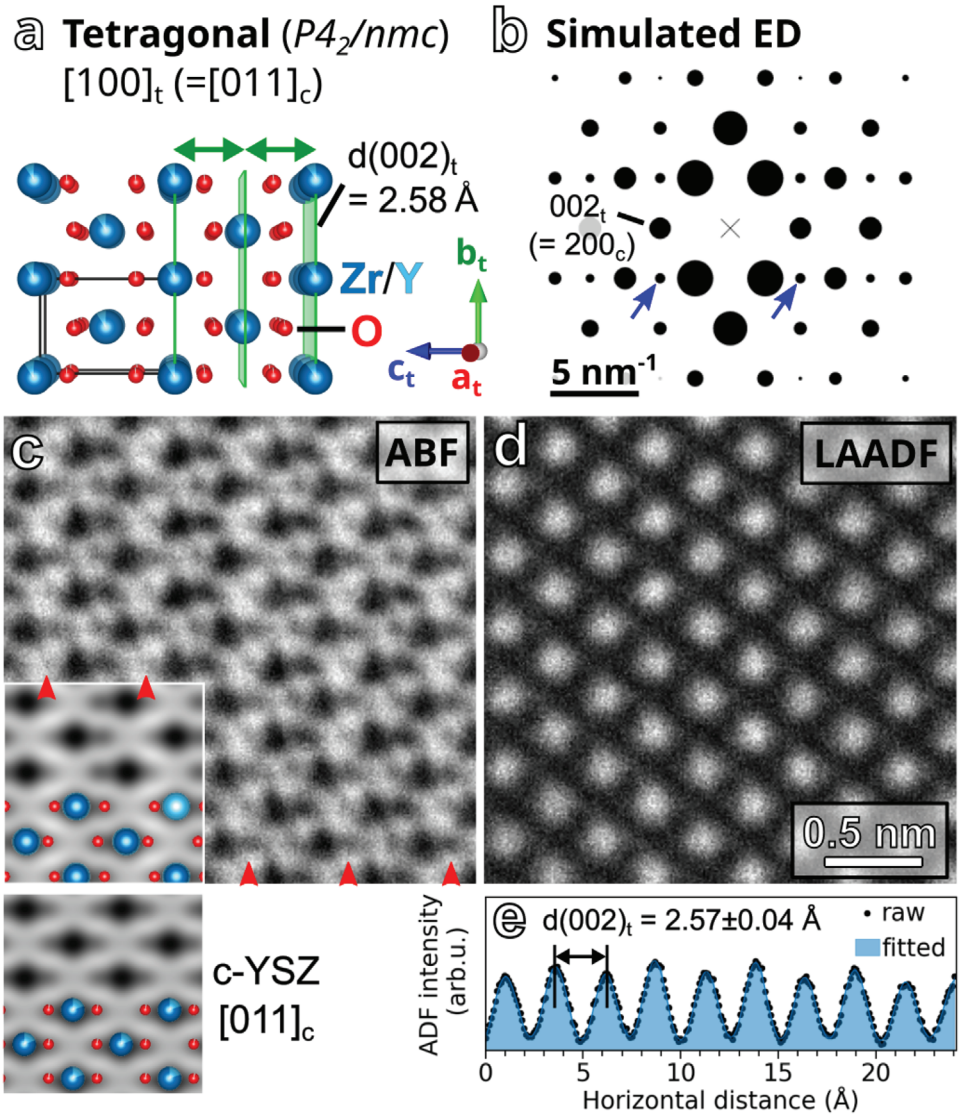

Figure 4. The tetragonal YSZ structure. a) Crystal structure representation of the tetragonal model (Space group: $P4_2/nmc$) along the $[100]_t$ (=$[011]_c$) direction. b) Kinematical simulation of the electron diffraction (ED) pattern along the same orientation of the tetragonal structure. c,d) ABF- and LAADF-STEM images for the tetragonal structure viewed along the $[100]_t$ (=$[011]_c$) direction, respectively. The "t" or "c" subscripts denote the tetragonal or cubic setting, respectively. For direct comparison, the projected models together with the simulated images are overlaid on top of the experimental STEM images. Additionally, a simulated ABF-STEM image for the cubic YSZ structure is also included. The red arrows in (c) indicate the oxygen-containing layers whose contrast appear brighter than other neighboring layers due to the difference in oxygen arrangements. e) Integrated intensity profile of the LAADF-STEM image in (d) along the horizontal axis and the calculated interatomic distances for the $d(002)_t$ (=$d(200)_c$) crystal planes.

repulsion with the adjacent cations leading to an expansion of the lattice.

By combining our microscopy observations with theoretical modeling, we now aim at deriving an atomistic model of this new ordered structure that partially develops in the vicinity of YSZ/LSM interfaces during 550 h time on stream. The experiments suggest that the ordered structure can be best described by three characteristic features: a two-fold modulation of $V_o^{\bullet\bullet}$, cations, and the $(200)_c$-equivalent lattice spacing. In the first attempt several candidates were considered including the tetragonal YSZ polymorph (space group: *P42/nmc*, see above), the pyrochlore structures $Y_2Zr_2O_7$ or $La_2Zr_2O_7$[52] (cubic, space group: *Fd-3m*), and the monoclinic ZrO_2 (space group: *P121/c1*). However, as shown in Figures S12 and S13, Supporting Information, these are all structurally incompatible with the characteristic features described above.

Our experimental results are similar to the structural model proposed by Wang et al.,[53] which is composed of ordered arrangements for Y/Zr cations and $V_o^{\bullet\bullet}$ in the 2×2×2 supercell of cubic YSZ. This compound has a composition of $Y_2Zr_2O_7$, which can explain the observed *dx* distance modulation of the Y/Zr cations within the electron micrographs. The adopted model was fully relaxed by density functional theory (DFT) calculations and refined into a monoclinic phase (space group: *P1c1*). Although we

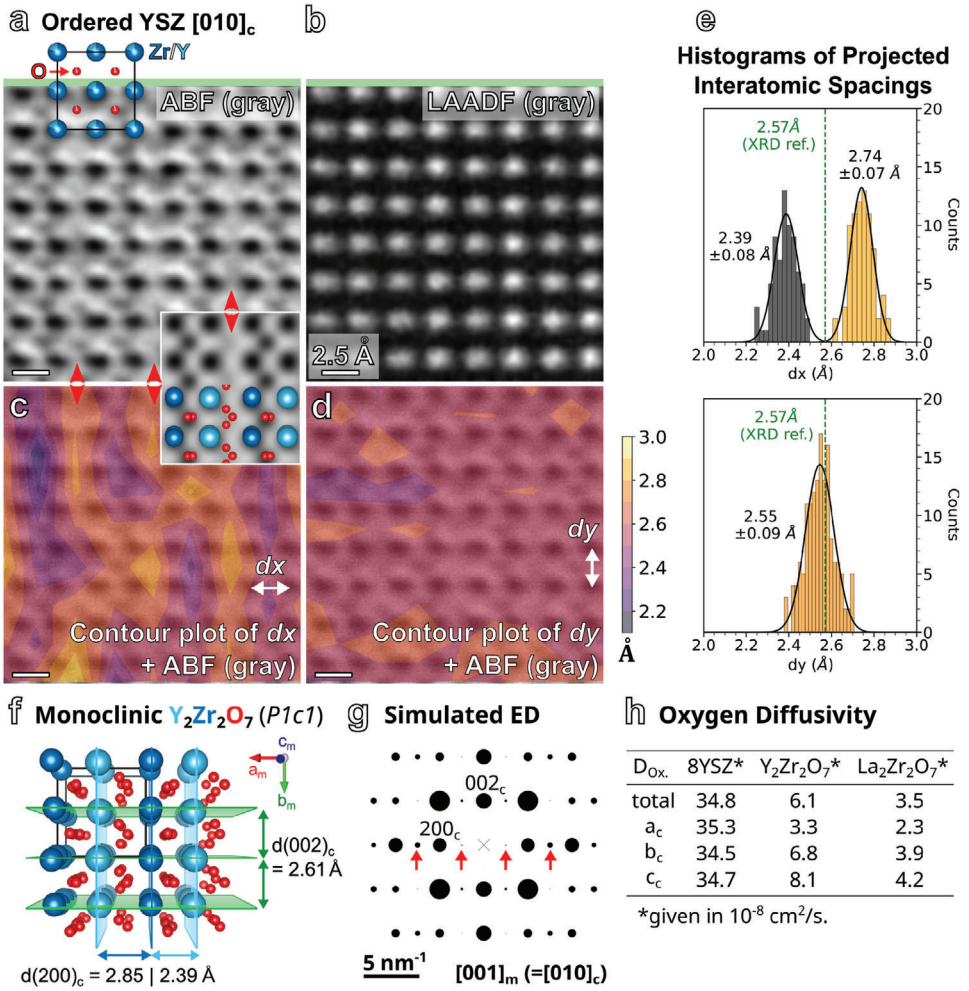

$D_{Ox.}$	8YSZ*	$Y_2Zr_2O_7$*	$La_2Zr_2O_7$*
total	34.8	6.1	3.5
a_c	35.3	3.3	2.3
b_c	34.5	6.8	3.9
c_c	34.7	8.1	4.2

*given in 10^{-8} cm^2/s.

Figure 5. On the structure of the pyrochlore-like nano-domains in YSZ. a) and b) represent ABF- and LAADF-STEM images acquired simultaneously from the ordered YSZ region along the $[010]_c$ orientation, respectively. To assist with visualization, the raw images were denoised using principal component analysis (PCA),[61] as shown in Figure S15 (Supporting Information). c) and d) reflect the corresponding contour plots displaying the spatial distribution of the projected interatomic spacings *dx* and *dy*. For the ease of viewing, the contour plots are overlayed on the gray background of the ABF-STEM image shown in (a). The red arrows in (a) and (c) indicate the vertical layers with vanishing oxygen contrast. e) Histograms of the projected interatomic spacing values *dx* and *dy* for the ordered structure statistically sampled from a larger region as shown in Figure S16 (Supporting Information). The green dashed lines indicate the averaged values obtained from XRD analysis. f) 3D view of the proposed model (Monoclinic, space group: *P1c1*) for the pyrochlore-like ordered structure after relaxation by DFT. Further details on the monoclinic model can be found in the crystallographic information file (CIF) presented in Section S9 (Supporting Information). For direct comparison, the projected models together with the simulated images are overlaid on top of the experimental STEM images in (a). g) Simulated electron diffraction of the proposed model along the $[001]_m$ (= $[010]_c$ of cubic YSZ) direction which reproduces the two-fold superstructure reflections (red arrows) observed in the previous FFT (Figures 3a). h) Oxygen diffusion coefficients at 900 °C obtained from MD simulations for YSZ and the proposed pyrochlore-like structures.

choose to display here the representative $Y_2Zr_2O_7$ model, other possibilities with $La_2Zr_2O_7$ or $(Y, La)_2Zr_2O_7$ compositions might also exist in the near interface region as a result of their similar structures and the high swapping probability between La and Y atoms in YSZ.[35] In fact, we also observed the Z-contrast alternation of cations in some cases (Section 8, Supporting Information), suggesting the contribution from La in the $(Y, La)_2Zr_2O_7$ structure ($Z_{La} = 57 > Z_{Zr} = 40$, $Z_Y = 39$). Further details of both models as well as a systematic comparison can be found in Section S9 (Supporting Information).

The proposed model (Figure 5f) exhibits various crystallographic features that are well in line with our microscopic observation. First, the interatomic spacings for the $(200)_c$-equivalent planes in the DFT-relaxed $Y_2Zr_2O_7$ bulk model alternate between 2.39 and 2.85 Å (Figure 5f), which matches within measurement uncertainties our experimental observation (Figure 5e). The expanded layers correspond well to the ordered arrangement of $V_o^{\bullet\bullet}$ in the model as depicted in Figure S19 (Supporting Information). Second, the clustering of oxygen vacancies into oxygen-deficient layers is responsible for the observed superstructure in the oxygen sublattice. Consequently, these layers, as indicated by the red arrows in Figure 5a,c, appear empty compared to the neighboring oxygen-containing layers in both the experimental and simulated ABF-STEM images. Third, the coexistence of ordered $V_o^{\bullet\bullet}$

and Y cations is seemingly imperative to maintain charge neutrality in the model when substituting Zr^{4+} by Y^{3+} cations.[49] This would result in a composition of $Y_{0.5}Zr_{0.5}O_{1.75}$ for the model as opposed to the bulk average composition of $Y_{0.15}Zr_{0.85}O_{1.93}$. Collectively, these modulated features contribute to the two-fold superstructure reflections as seen in the simulated electron diffraction of Figure 5g, in agreement with the previous FFT shown in Figure 3a.

Moreover, the ordering of oxygen into layers in the investigated material interrupts the 3D interconnected network of corner-sharing BO_6 octahedra, which is an important characteristic of the $A_2B_2O_7$ pyrochlore family.[54] The unique structure of this crystalline inclusion in YSZ also differs from those of other ferroelectric layered perovskites such as $La_2Ti_2O_7$, $Nd_2Ti_2O_7$ or $Ca_2Nb_2O_7$.[55] While it is not uncommon to observe $La_2Zr_2O_7$ pyrochlores (*Fd-3m*) in solid oxide cells at room temperature, in particular after heat treatments above 1000 °C,[18–20,56–58] the investigated pyrochlore-like structure observed in our study most likely represents a kinetically trapped intermediate or a nucleus towards the crystallization of pyrochlore. In such a scenario the surrounding YSZ bulk, which encapsulates the pyrochlore-like regions, might be important for their stabilization. Under the electrochemical high-temperature operating conditions, cations originating from the anode material might enter regions of the YSZ near the interface via the less rigid complexion by solid-state diffusion, in a concerted process with the influx of oxygen anions into the complexion. These cooperative processes effectively lower the energy barriers and promote the formation of the pyrochlore-like structure. This would also explain why the ordered $V_o^{\bullet\bullet}$ and cation layers tend to align preferentially with the diffusion direction of oxygen towards the interfacial regions (Figure 3a).

The proposed pyrochlore-like model provides a new view on a structural feature among the structural and compositional complexity displayed by the inclusions formed in YSZ. A more complex and complete scenario includes the occurrence of local areas with solid solutions of a wide range of compositions that can form in the presence of varying amounts of Y/La/Mn cations within the YSZ structure. Those local solid solutions may affect the spatial distribution of oxygen in the material and ultimately alter the oxygen transport to the complexion. The implications of such novel structural features that slowly emerge during cell operation are further investigated with molecular dynamics (MD) simulations. The computed oxygen diffusion coefficients for regular YSZ and pyrochlore-like structure are presented in Figure 5h. Compared to YSZ, the pyrochlore-like structure exhibits significantly lower oxygen mobility (one order of magnitude reduced D_{oxygen}). The oxygen mobility depends also on the crystallographic direction. Notably, the diffusion along the crystallographic a_c direction is less favorable compared to other orthogonal directions (b_c and c_c). As similar results are obtained for both $Y_2Zr_2O_7$ and $La_2Zr_2O_7$, this suggests the same impeding effect on the oxygen diffusivity for a structural scenario of $(Y, La)_2Zr_2O_7$, in which Y and La are intermixed along the ordered layers. The reduction of oxygen mobility within the pyrochlore-like inclusions is thus expected to further limit the oxygen ion flux to the active sites, which is five times more pronounced compared to tetragonal YSZ. Note, that the formation of the classical $La_2Zr_2O_7$ pyrochlore phase (*Fd-3m*) would cause a complete blockage of oxygen diffusion through the YSZ compared to the partially impeding effect of the pyrochlore-like structure (Figure S20, Supporting Information).

Note, electron diffraction of the bulk YSZ for the pristine and operated cells also shows the existence of superstructures which can be well-explained by the tetragonal YSZ according to previous reports[59,60] (Sections S10 and S11, Supporting Information). Due to the structural similarity (Figure S21, Supporting Information), the proposed pyrochlore-like model seemingly provides an alternative interpretation in some cases (Sections S10 and S11, Supporting Information) with an exception along the $[010]_c$ viewing direction (Figure S26, Supporting Information). This specific orientation allows an unambiguous differentiation between the two structures (Figures S26 and S21, Supporting Information). Therefore, we conclude that the tetragonal YSZ is mainly responsible for the superstructure observed in bulk YSZ while the coexistence of both phases (i.e. tetragonal YSZ and pyrochlore-like structures) occurs predominantly at the electrode/electrolyte interface of the operated cell (Figure 3).

In the near interface region, diffusion of La/Mn into YSZ causes a redistribution of the elements (Section S12, Supporting Information), which alters the local chemical compositions. Diffusion might also be responsible for the formation of the nano-sized ordered domains in this region. Consequently, the local enrichment of Y, which favors the pyrochlore-like structure is expected to be accompanied by regions of Y-depleted zones, which is in turn promoting the tetragonal YSZ structure[53] (Section S12, Supporting Information). This solid-state process is facilitated by the prolonged heating/biasing at elevated temperatures of the cells (Section S13, Supporting Information).

2.3. Mixed Ionic Electronic Conductivity

2.3.1. Diffusion at Interfaces and Its Role in the Oxygen Transport Properties

The finding of different secondary structures, including the tetragonal YSZ as well as the pyrochlore-like structure, is intriguing and demonstrates that cation diffusion through the solid from the LSM electrode into the YSZ electrolyte occurs during operation. This shows the existence of local diffusion paths leading to structural and compositional pluralism in the vicinity of the interface (Sections S12 and S13, Supporting Information), which also includes the presence of antisite defects due to cations occupying oxygen lattice sites in YSZ (Section S14, Supporting Information). The impact of such novel motifs on the function and degradation of the cell needs to be modeled and understood at the atomic scale, as each of them may contribute to the overall ionic transport differently. An atomic scale area including the LSM electrode, complexion, and the YSZ electrolyte is presented in **Figure 6a**. The complexion that forms between LSM and YSZ is characterized by an increased disturbance of the cation lattice and is approximately 1 nm thick (Figure 6a; Section S15, Supporting Information). A similar structure of the complexion with reduced long-range order has been also observed for the non-operated cell (Figure S37, Supporting Information). In line with our previous finding, the pre-treatment at a high temperature (1150 °C) prior to operation has a beneficial effect on its

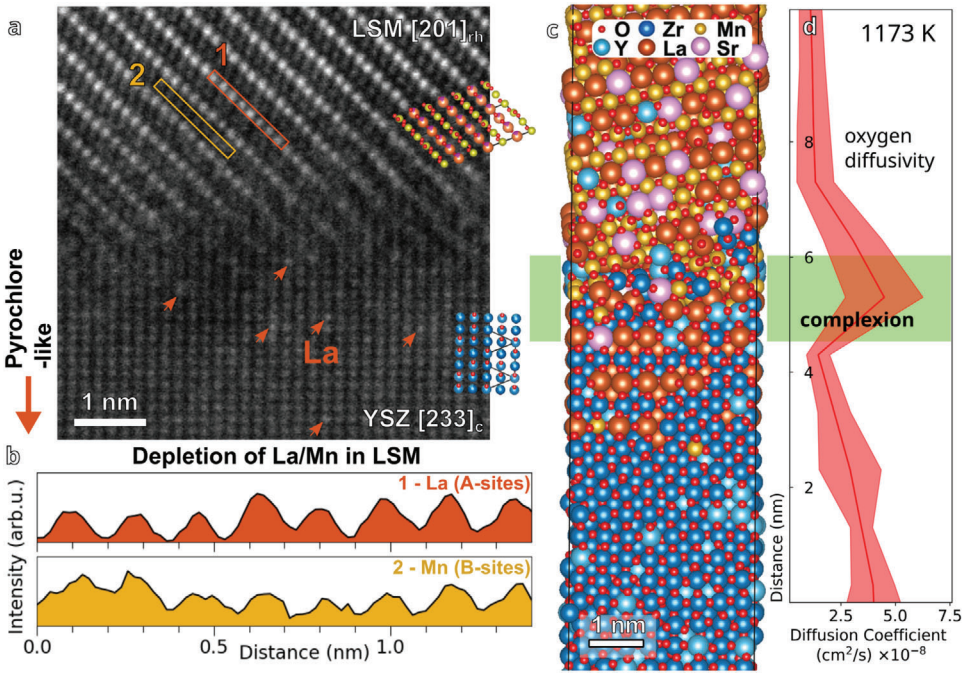

Figure 6. Atomic structures at the interface between LSM and bulk YSZ electrolyte. a) HAADF-STEM image with both the LSM and YSZ being well oriented along the low-index zone axes, LSM $[201]_{rh}$ and YSZ $[233]_c$. A nano-domain of the secondary structures in the vicinity of this interface is outside of the current view as indicated by the downwards arrow in (a) and can be seen more clearly in Figure S17 (Supporting Information). b) Two intensity line profiles (denoted 1 and 2 in (a)) for two selected atomic rows of the La- and Mn-sites, respectively, in the LSM perovskite structure. c) Structure of the complexion obtained from Monte–Carlo simulations. d) Spatially resolved oxygen anion diffusion coefficient across the LSM/YSZ interface from molecular dynamics simulations at 1173 K. To simplify comparison, the alignment is the same as in c, and the complexion of 1.4 nm thickness is indicated by a green area middle with its middle at 5.3 nm.

formation.[35] In general, the detailed structure of the complexion depends on multiple factors, such as the crystallographic misalignment or the inter-diffusion profiles of the abutting LSM and YSZ phases. These are not finally determined by the initial sintering of the materials but keep evolving under reaction conditions during operation. For instance, the ongoing redistribution of cations is directly evidenced by the intensity variations in Z-contrast imaging shown in Figure 6 that result from the depletion of La/Mn on the LSM side close to the interface region and the concurrent enrichment of La in the complexion at the YSZ side. It is further corroborated by the elemental EDX line profiles across the LSM/complexion/YSZ region (Figures S30 and S33, Supporting Information). The same atomic scale electron micrograph further suggests that La can occupy Zr/Y sites in the neighboring YSZ region with the characteristics of a solid solution that may eventually promote the formation of the secondary structures. Note that at this location of the SOEC cell, a nano-domain of the secondary structures was found further away from the interface (Figure S17, Supporting Information) as compared to other investigated regions of the same sample (e.g. Figure 3).

To investigate the influence of such changes of the local chemistry on transport properties in the vicinity of the complexion, Monte–Carlo simulations were conducted to generate ensembles of structural models. A representative example is presented in Figure 6c. The model highlights the effects of cation diffusion on the interface structure and is in good agreement with the experimental findings. On the LSM side, La as well as Mn ions are replaced by Zr/Y, which is, for instance, corroborated by the measured fluctuations of the signal intensities along the rows of La- and Mn-sites close to the LSM/complexion edge (Figure 6b). Conversely, on the YSZ side, La/Mn migrates into the material causing the formation of solid solutions and the promotion of secondary structures such as the tetragonal YSZ and the pyrochlore-like structures.

Molecular dynamics (MD) simulations with these structural models reveal (Figure 6d; ≈4 nm; Figure S38, Supplementary Information) that La/Mn diffusion into YSZ has a detrimental effect on the oxygen diffusivity close to the interface of the complexion with the YSZ. On the contrary, the depletion of La/Mn and the incorporation of Zr and Y into LSM increases the oxygen diffusivity within the solid electrode region (see Figure 6d ≈6–8 nm). This finding suggests that the active area is not only located in the complexion, but it can grow into regions of the LSM near the interface, mediated and adjusted by the chemical versatility of the complexion.

2.3.2. Electron Conductivity

Oxygen ion and electron conductivity are the most important properties that contribute to the superior efficiency of SOECs. As shown above, the local chemical composition significantly influences the oxygen ion conductivity. Next, we set out to explore the influence of the local composition on the electron conductivity of the bulk oxides at complexion near regions. For this purpose, we used electron energy loss spectroscopy (EELS) to probe the

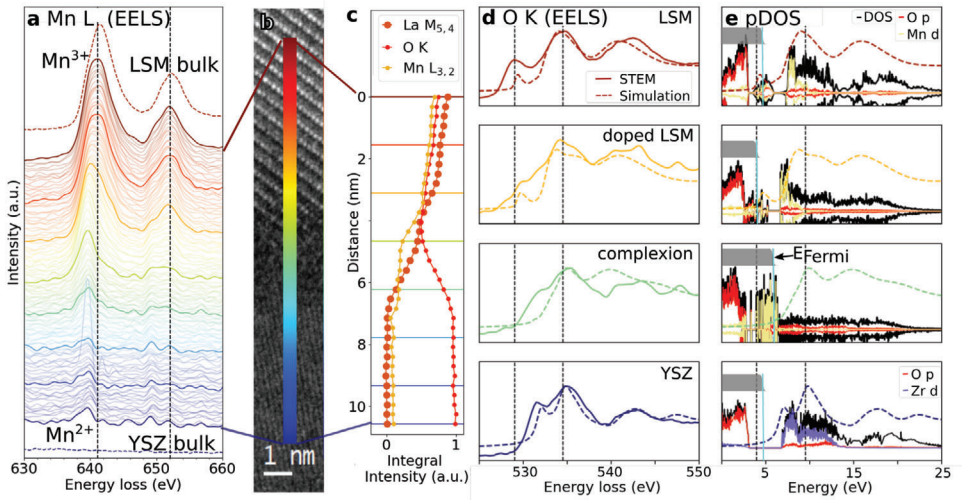

Figure 7. Electronic structures at the LSM/complexion/YSZ interfaces. a) Sequential series of the as-acquired EELS spectra for the Mn $L_{3,2}$ core-loss edges. Each spectrum is spatially 0.1 nm apart and color-coded according to its position on the line scan shown in (b). For comparison, the reference spectra of the bulk LSM and YSZ taken far away from the LSM/YSZ interfaces are also included as dashed lines. Note, the complete EELS dataset including O K and La $M_{5,4}$-edges is provided in Figure S39 (Supporting Information). b) Survey HAADF-STEM image with a colorbar indicating the positions of the EELS spectra across the complexion. c) Integral intensities for La $M_{5,4}$-, O K- and Mn $L_{3,2}$-edges as a function of distance across the LSM/YSZ interface. d) Experimental (solid) and simulated (dashed) O K-edges for LSM (dark red), Y-doped LSM (yellow), complexion (green) and YSZ (blue). Dashed black lines indicate the position of the first and second maximum of the peaks in LSM to ease comparison of the different structures. e) Simulated O K-edges with respective projected DOS (pDOS). The Fermi energy (E_{Fermi}, turquoise solid line) and the corresponding Fermi–Dirac distribution (solid gray) at 1000 K is shown as inset.

unoccupied state of the electronic structure across the same LSM/YSZ interface as in the previous section (see Figure 6). A series of spatially resolved EEL spectra of the Mn $L_{3,2}$-edges recorded from the LSM over the complexion to the YSZ are shown in **Figure** 7a and their correlation to the position in the sample is given in Figure 7b.

From these Mn $L_{3,2}$-edges the local composition and oxidation state of manganese across the complexion and into the YSZ was derived. The Mn $L_{3,2}$-edges of bulk LSM predominantly resemble those of Mn^{3+} species. They successively shift to lower energies towards the complexion, indicating the reduction of Mn^{3+} to Mn^{2+}. This change in oxidation state is also evidenced from the change of Mn L_3/L_2 peak ratios as described in more detail in Section S18 and Figure S40 (Supporting Information). Figure 7c shows the integral intensities of La $M_{5,4}$ -, O K- and Mn $L_{3,2}$-edges across the complexion. The Mn and La intensities decrease before entering the complexion, which translates to a declining cation concentration. While the La content decreases continuously over the entire complexion, the Mn content remains constant in the same area and decreases again in the YSZ electrolyte. Yet, Mn is still detectable in approximately the initial 3 nm of the YSZ. In contrast to the behavior of the cations, the integrated intensities of the O K-edges show a local minimum in the complexion, which is significantly lower compared to the confining bulk phases. A similar feature is also observed from the EDX line profile in Figure S30 (Supporting Information). This observation could be a result of the lower density of the complexion, but also of the lower oxidation state of Mn, which requires fewer oxygen ions for charge compensation. The increase in oxygen content towards the YSZ electrolyte could have been caused by diffusional contributions from the electrolyte into the complexion. It is evident that the concentration gradient of the elements along the complexion and the change of the oxidation state of Mn significantly influences the local electronic structure. The trend is consistent with the previous study by Backhaus–Ricoult et al.[31,32] However, our results provide a more detailed view on the electronic transitions across the LSM/YSZ interface, which was further improved by applying theoretical modeling.

Figure 7d shows the experimental and simulated O K-edge spectra of LSM, doped LSM, the complexion, and YSZ. Relevant dopant concentrations for the simulation were obtained by a design of experiment (DoE) approach and can be found in Figures S41 and S42 (Supporting Information). For all model structures, the simulations agree well with the experiment, and reproduce all prominent features of the corresponding experimental EEL spectra. The largest difference between the O K-edge of LSM and YSZ is the absence of the pre-peak at 529 keV. As suggested by the projected density of states (pDOS) in Figure 7e, this peak arises from the excitation of core electrons into the unoccupied hybridized states of O p- and Mn d-orbitals. Interestingly, this peak also appears directly at the Fermi level of LSM, which is indicated by the turquoise solid line marking the edge of the Fermi-Dirac distribution at operation temperature, which is displayed as a grey rectangle. These unoccupied states are positioned exactly at the lower edge of the conduction band and thus close the band gap. Consequently, the existence of this pre-peak in the O K-edge is characteristic of electron conductivity. As illustrated in Figure 7e, this pre-peak is present not only in the pure LSM phase, but it can be also observed in the compositionally variable LSM part close to the complexion and in the EEL spectrum of the O K-edge, which was recorded from the complexion. Combining this information with the results of the MD

simulation mentioned above, which revealed an increase in oxygen ion conductivity in regions of the LSM that are close to the complexion, we conclude that this region, which is approximately 1 nm thick, as well as the complexion itself are mixed ion and electron conductors.

Note that the observation of reduced Mn^{2+} species at the anode side might be surprising for an OER catalyst. We tentatively relate these to sites that can structurally accommodate the local changes upon variations in the manganese oxidation state. We observe them here in a sample that during EELS recording is not electrically biased in the same way as under operating conditions. This also hints at different prevailing electron conductivity mechanisms in the LSM bulk and in the MIEC region. LSM is a band electron conductor, in which free electrons are delocalized. However, the finding of Mn^{2+} species in the MIEC region in a sample at ambient conditions (room temperature, no bias, no reaction atmosphere) suggests that in the MIEC the electrons form mobile polarons under reaction conditions and are due to defects. In such a scenario electron conductivity would be accomplished by polaron hopping. Under operation conditions Mn^{3+} species are expected to be predominant and Mn^{2+} sites to occur transiently during polaron hopping. However, upon cooling and without bias the free electrons are trapped on manganese cations in local environments that support the most stable Mn^{2+} polaronic species.

In previous reports, it has been concluded that the MIEC effect can even reach into the neighboring YSZ due to the solid solution that can form between Mn cations and YSZ.[31,32,62] However, this was not confirmed by the detailed EELS analysis in our study. In LSM/YSZ-based SOECs, the electrochemical activity is generally associated with the number of TPBs within the cells.[5] The TPB describes the intersection of the pure ion conductor (YSZ), the pure electron conductor (LSM), and the gas phase. Faster reaction kinetics can be achieved if the active area around the TPBs is increased. The MIEC domains unveiled in our study significantly enlarge the active area of SOECs, as not only a 1D line along the TPB, but also the complexion and the adjacent LSM regions fulfill the necessary requirements for efficient oxygen evolution. Hitherto, MIEC has not been described for LSM derived SOECs, but it is a well-known fact for lanthanum strontium cobalt ferrite (LSCF) which is an intrinsic MIEC material.[63,64] As such the complexion may be formed to avoid the energetically unfavored abrupt extinction of the electron and oxygen conductivities similar to the interfacial layer that forms at solid–liquid interfaces under electrochemical biasing.

2.4. The Effect of Solid-State Chemistry on the SOEC Performance

2.4.1. Established Mechanisms for Cell Deactivation

The tight interplay of atomic scale imaging with theoretical modeling applied to an operated SOEC is unprecedented. Our example demonstrates the importance of obtaining the spatial and atomic scale information of functional solids in order to understand the origin of their function. Active and inactive regions can coexist within the same sample and can be separated by only a few nanometers. In this regard, local solid state chemistry that occurs under reaction conditions self-adjusts the interfacial properties of the SOECs by fine-tuning their complex structural and compositional motifs. Ideally, this results in synergistic ion and electron transport properties that might be beneficial for the performance of the device, however, as shown above, detrimental effects do also occur which lead to a reduction of the oxygen supply by La/Mn diffusion into the YSZ and the additional formation and growth of secondary structures. Strategies to mitigate the undesirable formation of zirconate phases such as $SrZrO_3$ and $La_2Zr_2O_7$ pyrochlores have been proposed involving the control of the LSM stoichiometry and the La/Sr ratio (i.e. $(La_{1-x}Sr_x)_{1-s}MnO_3$ with $0.05 \leqslant s \leqslant 0.15$ and $0.15 \leqslant x \leqslant 0.30$[65]). This is well adapted in our case and close to the optimum bulk composition of $(La_{0.8}Sr_{0.2})_{0.95}MnO_{3-\delta}$. This composition of the anode also explains the absence of other zirconate phases in our cell.

In SOEC operation, delamination of the LSM/YSZ interface is one of the most prominent causes of deactivation.[11,12,66,67] This form of material failure is catastrophic to cell functionality and must, therefore, be avoided. The delamination is often attributed to the build-up of internal partial pressure and the subsequent void formation along interfaces and grain boundaries, especially under high polarization,[12,68] which eventually evolve into cracks.[66,68,69] In addition, the weakening of interfacial structures via the formation of secondary phases[18,23,70,71] or local stress/strain[72] has been regarded as other possible cause. Notably, these different scenarios seem to share a common link to the underlying effect of cation migration. To a lesser degree, cation segregation towards the surface, especially for Sr,[9,36] in combination with other volatile surface species, might also lead to the blockage of active sites,[9,36,73–75] thus lowering the cell performance over time. While this thermodynamically driven effect has been shown to be reversible for some air electrode (anode) materials such as $La_{0.8}Ca_{0.2}MnO_3$, the widely studied LSM does not show this reincorporation due to the large mismatch in cationic sizes ($r_{Sr} > r_{La}$).[21,76] As shown in our recent study,[35] cation migration already occurs during cell preparation and is expected to dynamically evolve with the ongoing electrochemical operation. Therefore, an atomistic understanding of this effect in the early stage of operation is essential to unravel the genesis of cell deactivation. This would provide the basis for design strategies aiming at preventing the onset of the more severe deactivation features on the micro-scale or above. All of these performance degrading effects and their long-term symptoms observed at non-atomistic length scales are ultimately related to cation diffusion at the atomistic YSZ/LSM interface which differs from the bulk behavior of the two materials. A positive effect of cation diffusion on the performance as it was also found in our study with the MIEC formation on the LSM side during SOEC operation has not yet been reported and requires that advanced optimization strategies need to be developed that strive to balance between detrimental and advantageous solid-state processes. In the following, we will discuss findings that indicate that this goal might be achievable.

In view of previous literature[9,11,12,36,66–69] and our recent findings, we hypothesize the following atomistic scenario leading to the deactivation of SOEC at 800 °C and −0.3 A·cm^{-2}: A non-operated, pristine cell has a finite width complexion with a spandrel-like evolution towards the TPB at the nanoscale,[36] as

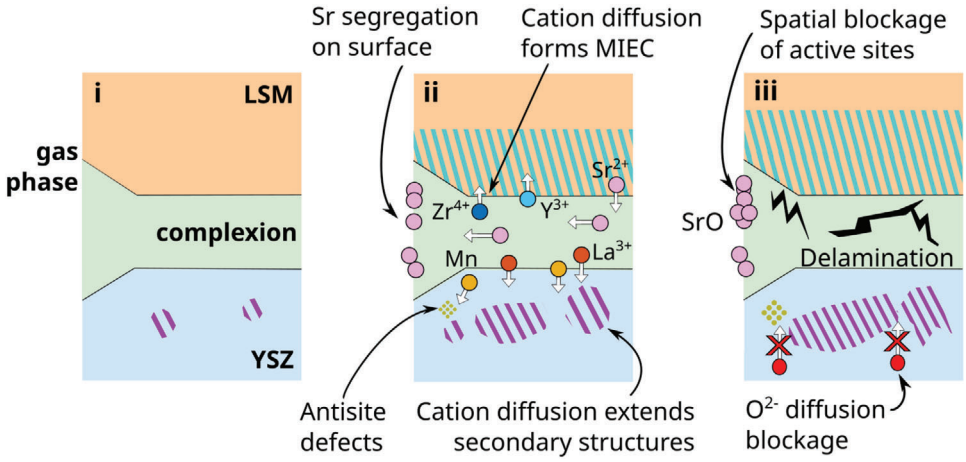

Figure 8. Atomistic insights into the thermal electrochemical aging of SOECs. Schematic showing a hypothetical pathway leading to the structural degradation of SOECs with time on stream. The pathway is derived by combining results from previous reports[9,11,12,36,66–69] and this study. Schematic structure of i) a non-operated, pristine cell, ii) intermediate stage of the cell, at which cation diffusion causes MIEC formation and growth at the LSM side extending the active area for OER. In addition, cation diffusion promotes the additional formation and growth of a solid solution of La/Mn, secondary structures and antisite defects in the YSZ decelerating the diffusion of oxygen. iii) State of a deactivated cell with blocked oxygen ion diffusion, spatially blocked active areas and a delamination-prone complexion due to cation segregation.

we illustrate in stage i) of **Figure 8**. Already at this stage, first nano-domains of the secondary structures have been found in the YSZ, especially in the small grains of the LSM/YSZ anode composite (Figure S8, Supporting Information). Note, at the interface between LSM and bulk YSZ electrolyte, i.e the area, which is the most susceptible to delamination,[66,68,69,76] secondary structures were hardly observed in the pristine cell (Figures S6 and S7, Supporting Information). The initial secondary structures formed might be self-limited in size owing to the availability and depletion of vicinal Y cations.

Upon operation as shown in panel (ii) of Figure 8, the diffusion of cations across the LSM/YSZ interface sets in to form a solid solution of La/Mn on the YSZ side. This way the oxygen diffusivity in the YSZ is impeded as shown in the MD simulation of Figure 6d. Cation diffusion from the LSM to the YSZ not only promotes the additional nucleation and growth of the secondary structures, but also the formation of antisite defects close to the LSM/YSZ interface (Section S14, Supporting Information). Consequently, the supply of oxygen ions to the active area is severely reduced. In addition, Sr segregation leads to the formation of strontium oxide (SrO) at the surface and partially blocks the accessibility of the active sites.[36] The combination of these changes in the local composition and structure on the anode side is detrimental for the lifetime of the SOEC. Notably, these effects might be exaggerated by a minor contribution from the cathode side of the SOEC based on the observed DRT peak shoulder at ≈400 Hz (Figure 2c; Figure S4 c, Supporting Information). Together they might be responsible for the overall increase in the cell voltage under current load (Figure 2a).

In addition, the diffusion of cations also leads to the formation of a MIEC in the interface near region of the LSM, which grows with time (see Section S21, Supporting Information for a comparative analysis between cells operated for 120 and 550 h). This effect increases the active area and oxygen diffusivity within important sample regions (stage ii) of Figure 8), and thus counterbalances the overpotential of the cell. Consequently, the MIEC effect might be responsible for the declined deactivation rate of the cell voltage after 50 h of operation (Figure 2a).

Such a decrease in cell voltage was not observed for all our investigated cells (compare Figure S3 a, Supporting Information). These varying behaviors of the cell voltage might be explained by the described interplay of cation diffusion and solid state reactions at different time on stream in addition to the thermal history of the cells. Nevertheless, the negative effects seemingly dominate, contributing to a constant increase of the cell overpotential, which ultimately leads to deactivation. Although we did not observe any void or crack formations up to ≈550 h of operation, it is anticipated that a weakened LSM/YSZ non-epitaxial interface might eventually result in delamination,[11,12,66,67] as illustrated in stage iii) of Figure 8, which might set in at longer times of operation.

2.4.2. Mitigation Strategy for Cell Deactivation

We propose that in order to improve the long-term performance of the SOEC, it is important to maintain the cell in a stable state that best mimics the structural situation after 200 h of operation. This state would reflect a frustrated phase transition, in which the system is most active. Any changes in the local chemistry and parameters will gradually lead to the completion of the phase transition and to deactivation. Keeping this point over the long-term requires precise control of the solid-state chemistry and energy barriers that trigger the interdiffusion of cations after performance-enhancing structural features such as the MIEC have been formed. This is not a trivial task as it would require the formation of suitable barrier layers at the YSZ and LSM solid–solid interfaces. A prerequisite for this layer is that it forms only after 200 h of operation under harsh reaction conditions, and is stable and thin enough to not affect oxygen and electron diffusion. In an attempt to control cation diffusion, Graves et al. previously demonstrated that cyclic operation between electrolysis

(1 h) and fuel-cell (5 h) modes significantly reduces cell deactivation up to 4000 h of operation.[43] In light of our findings, this can be attributed to the effect of controlled cation diffusion at the LSM/YSZ interface as it reduces the formation and accumulation time of oxygen-impeding phases, such as the tetragonal-YSZ and the pyrochlore-like structures. However, this approach requires complex setups and also shortens the effective SOEC operating time. Alternatively, cation diffusion might be controlled by interfacial doping or by covering the interface with a nanometer-thin layer of compatible materials already during synthesis. This would help to reduce contact areas and to slow down the onset of detrimental solid state chemistry. In line with this hypothesis, improvements in the cell stability have been reported for a coating layer prepared by sol-gel synthesis (≈1 µm Mn-doped YSZ)[77] or solution infiltration (≈60 nm Co-based perovskite).[78] The usage of gadolinium-doped or yttrium-doped ceria (GDC/YDC) micrometer-thick layers, which is common for preventing the interaction between LSCF and YSZ,[69,79,80] might also be transferable to the LSM/YSZ system. Nevertheless, successful studies on interfacial engineering show, that such rather thick layers are not suitable to achieve the desired interfacial properties. As an alternative, atomic layer deposition (ALD) was used to coat the surface of solid electrolytes for battery application in the nanometer regime, which gave promising results in terms of performance and lifetime enhancement.[81–83]

For SOCs, studies on a synthetic coating of the interface of electrode or electrolyte involve the deposition of relatively thick layers (100–1000 nm).[77,84] Although these materials could show an improvement in the cell performance, these modified cells still degraded rapidly. We anticipate, that the large thickness of these coatings is unsuitable to stabilize the desired cell properties. Nano-sized coatings could be epitaxially grown onto the underlying bulk phase, which could act as template for the structure of the thin film. A potential candidate is ZrO_2 which when adequately deposited can retain the cubic structure of YSZ and no additional stress and strain may be induced into the system, while increasing the diffusion barrier for La as demonstrated in Figure S44 (Supporting Information). Annealing under controlled oxygen partial pressure may adjust the oxygen vacancies in this adlayer and thus the oxygen diffusivity. Alternatively, other porous nano-scale coatings may be envisioned, such as the gentle deposition of laterally condensed TiO_2 layers, which could trap the migration of cations in an in situ generated diffusion-blocking layer of Mn-substituted strontium lanthanum titanate, which has been used as fuel electrode material.[85] Doping with other ions such as Ga, Mo, Bi or Co, whose lanthanum strontium titanates are used as SOC electrodes,[86,87] are also possible. Overall, the high complexity of the system and the simultaneous occurrence of different effects require more detailed studies, ideally with more controlled *operando* or quasi in situ systems.

3. Conclusion

In summary, we have shown that local solid-state chemistry at the anode/electrolyte interface of LSM/YSZ derived SOECs can be a bane and a boon for the long-term stability and performance. On the one hand, cation diffusion might be important to generate in situ a MIEC layer at the LSM/complexion edge leading to enhanced electron and oxygen ion conductivity. On the other hand, the La/Mn diffusion into the YSZ promotes a solid solution of these cations in YSZ as well as the additional formation and growth of secondary structures and antisite defects that are detrimental for the oxide ion supply. Thus, the formation and growth of these defective structures in YSZ have to be mitigated. Our results are based on a detailed chemical electron microscopy study that is paired with in depth theoretical modeling. This way, we provide a comprehensive and unprecedented local view on the structure of SOECs and discuss the origin of their activation and deactivation at the critical anode/electrolyte interface, which we derive from the local solid-state chemistry. This study emphasizes the benefit of combining atomic scale experiments and theory. It further stimulates the theory-driven development of prospective aging and *operando* experiments to reveal the structural changes in interfacial regions and demonstrates the importance of a detailed real structure analysis to unravel any structure-performance relationships. It suggests novel paths forward toward rational design concepts of SOECs focusing on enhancing their lifetimes.

4. Experimental Section

Single Cell Preparation and Electrochemical Characterization: The single cells were fabricated by using commercial NiO-8(YSZ supported half-cells (NiO-8YSZ || 8YSZ, CeramTec, ASC-10C type, d = 20 mm and thickness 400 µm, electrolyte thickness = 10 µm). To prepare the oxygen electrode, LSM ($(La_{0.8}Sr_{0.2})_{0.95}O_{3-\delta}$) powder (Fuel Cell Materials, USA) and an LSM + 8YSZ (50:50) ((8 mol% Y_2O_3 in ZrO_2) powder (Tosoh, Japan)) composite were separately mixed in a binder solution comprising 3 wt% ethylcellulose (binder) dissolved in α-terpineol (dispersant). Slurries were then mixed using a planetary vacuum mixer (THINKY Mixer ARV-310) and subsequently homogenized for ≈30 min by roll milling. First, an LSM + 8YSZ composite layer (thickness ≈25 µm and diameter 10 mm) was printed on the NiO-8YSZ || 8YSZ half-cell and after drying at 80 °C, an LSM layer (thickness ≈25 µm, diameter 10 mm) was printed over LSM + 8YSZ composite layer. The final sintering was performed at 1150 °C for 1 h in air, with a heating rate of 2 °C min^{-1}. The active area of the cells was 0.785 cm^2. For the measurement, Pt grid (1024 cm^{-2} mesh) was used as current collector for oxygen electrode and Ni grid (1024 cm^{-2} mesh) was used for the fuel electrode. The electrochemical measurements were performed using a NorEcs Probostat setup with two electrodes (four wires) to characterize the single cells. After placing the cells in the set-up, the cells were heated up to 900 °C (with 1 °C min^{-1}) under N_2 flow on fuel electrode side and air flow on oxygen electrode side. The NiO-8YSZ was then gradually reduced to nickel (Ni-8YSZ) by stepwise substitution of N_2 by dry hydrogen (H_2). After complete reduction of the cells, the gas flow was switched to humid conditions i.e. to a mixture of 50% H_2 and 50% H_2O (4.5 L·h^{-1} H_2 + 4.5 L·h^{-1} H_2O on fuel electrode side and 9 L·h^{-1} air, on the oxygen electrode side, respectively). The cell temperature was then lowered to 800 °C. Finally, long-term stability tests of the single cells were carried out at 800 °C with a current density of −0.3 A·cm^{-2} under a gas mixture of 50% H_2O and 50% H_2.

Electrochemical impedance spectroscopy (EIS) was performed under potentiostatic control with 50 mV ac amplitude from 110 kHz down to 110 mHz with 21 frequencies per decade using an IviumStat (Ivium Technologies, Netherlands) potentiostat/galvanostat with integrated frequency response analyzer module. For SOEC #1, impedance diagrams were recorded under OCV at the beginning and the end of the long-term test (Figure 2). For SOEC #2, the impedance was measured in situ without interrupting the constant current load of −0.3 A·cm^{-2} (Figure S3, Supporting Information). The quality of the impedance spectra was determined and validated using the Kramers–Kronig transformation test. As the Nyquist plot is rather convoluted the impedance data were transformed into the time domain to plot the distribution of relaxation times

(DRT). This allows the separation of relaxation times within a complex reaction mechanism. With this technique the number of time constants within the impedance data can be determined.[88–90] For this, the complex impedance diagrams were fitted using an equivalent circuit models by means of the RelaxIS software.

Sample Preparation for Electron Microscopy: Electron-transparent lamellae containing the LSM/YSZ interfaces of the bulk cell were prepared using a Helios NanoLab G3 FIB-SEM DualBeam system (ThermoFisher Scientific, USA). It provides gallium ions with energies up to 30 keV. Special care has been taken to minimize damage and redeposition of the removed materials onto the lamellae's side walls, by additional polishing steps at low ion energies of 5 and 2 keV, respectively. Additional Ar-ion beam milling was carried out on a Dual Mill 600 instrument (Gatan Inc.) to remove possible FIB-induced artifacts such as amorphous layers.

Electron Microscopy: Structural characterization was performed using a Cs-corrected JEM-ARM200F scanning transmission electron microscope (Jeol, Japan) at an accelerating voltage of 200 kV. In the STEM setting, the bright field (BF-STEM), annular bright field (ABF-STEM), low-angle and high-angle annular dark field (LAADF-/HAADF-STEM) imaging modes were used. ABF-STEM images were recorded on a BF detector with the inner/outer collection angles (8–18 mrad) limited by the beam stopper and a 3 mm bright field aperture, respectively. This technique is sensitive to image light elements in the vicinity of heavy elements as it has been, for instance, successfully used for imaging oxygen/nitrogen[91,92] or even hydrogen atoms[93] in crystalline materials. The Gatan ADF detector angles corresponding to the LAADF and HAADF-STEM modes are 27 mrad $< \theta <$ 61 mrad and 53 mrad $< \theta <$ 118 mrad, respectively, based on the calibration from another machine of the same model.[94] Additionally, STEM measurements were performed on a Cs-corrected Themis Z 80–300 (ThermoFisher Scientific, USA) at GFZ German Research Centre for Geosciences. The instrument was operated at 300 kV and equipped with a Gatan Continuum 1065 electron energy loss spectrometer.

In addition to Z-contrast, the LAADF signal also gives rise to effects involving de-channeling of the electron beam such as strain fields or phonons.[95,96] Other general settings include a convergence angle of ≈16 mrad and a probe current of 4.3 pA. To minimize sample drifts during imaging, a series of 20–30 rapidly scanned STEM images were first acquired with a dwell time of 2.4 µs per pixel. By cross-correlating these images in the post-processing steps, the drift-corrected images with sufficient signal-to-noise ratios were then obtained.

Electron energy loss spectroscopy (EELS-STEM) was acquired in the DualEELS mode with a Gatan Quantum ER imaging filter. The collection angle for the EELS spectrometer was 35 mrad. Spectrum images were collected with a probe current of 32 pA and the dwell time was 0.25 s per pixel. Each spectrum of the line scan series was averaged over a distance of ≈10 nm parallel to the LSM/YSZ interface, effectively minimizing the effect of beam damage. In the post-processing steps, the integral intensities for La $M_{5,4}$, O K and Mn $L_{3,2}$-edges were obtained by integration of the core-loss edge intensity over an energy window of 40 eV from the edge onset after pre-edge background subtraction. The oxidation states of Mn were estimated from the corresponding Mn L_3/L_2 peak ratios. The results were complemented by further analysis with MgEdgeNet, a machine learning toolbox for decomposition of the mixed Mn oxidation states.[97] A comparison between the two methods is given in Figure S40 (Supporting Information).

Energy dispersive X-ray spectroscopy (EDX-STEM) was measured with a Talos F200X (ThermoFisher Scientific, USA) at 200 kV. The instrument was equipped with four silicon drift detectors in a Super-X design, enabling a total solid angle of 0.9 sr. EDX spectrum images were acquired with a dwell time of 25 µs per pixel, a step size of 0.64 nm per pixel, and a probe current of 119 pA. Additionally, EDX-STEM measurements at the atomic scale were performed on the JEM-ARM300F2 (JEOL) at the Center for Electron Microscopy (ZELMI, TU Berlin). The measurements were performed at 50 pA under 200 kV using a 2.2 sr EDX detector.

Electron backscatter diffraction (EBSD) maps were acquired at 15 kV and ≈1 nA using a Zeiss UltraPlus equipped with Oxford Instruments Symmetry EBSD camera.

The Dr. Probe software was used for the simulation of STEM images,[98] assuming a source size of 40 pm (half-width at half-maximum). The input cells (≈20 nm in thickness) for simulation were based on the structure models optimized with DFT. The detector angles were taken from the experimental setting values. In addition, kinematical simulations of the electron diffraction were performed with the ReciPro software.[99]

X-Ray Diffraction: The X-ray diffraction (XRD) measurements were performed in Bragg–Brentano geometry on a Bruker AXS D8 Advance A25 theta/theta diffractometer, using Cu $K\alpha_{1+2}$ radiation and a position sensitive energy dispersive LynxEye XE-T silicon strip detector in high energy resolution mode (no Ni filter required).

Monte Carlo and Molecular Dynamics Simulations: Monte–Carlo based simulations were performed to mimic the sintering process done during cell production. The protocol for cations swaps and intermediate MD simulations for this sintering process can be found in previous work.[35] For this study, new, larger simulation cells consisting of 14 228 atoms in total (9162 O, 835 Mn, 167 Sr, 510 Y, 2946 Zr, and 668 La) were constructed, which enabled to capture more long-range effects. A classical force field merged from refs. [100] and [101] as described in ref. [35] was used. Sixteen interfacial cells were constructed with random doping, from which the 6 with the lowest potential energy were selected to perform ionic diffusion calculations. The diffusion coefficients were calculated for NPT relaxed cells at 1173 K and atmospheric pressure. For this, initial cells were relaxed with CASTEP,[102] constructed supercells of ≈10 000 atoms and performed MDs of 1 ns each with 10 ps equilibration time and a 1 fs timestep. To obtain the diffusion coefficient along the complexion, the lag time mean square displacements of 1 nm wide sections was computed. Simulation conditions were the same as mentioned above. All diffusion coefficients averaged over the computed 6 structures.

Design of Experiment for Structure Generation: In order to obtain small, periodic cells that capture the chemical environment of the complexion best, a design of experiment (DoE) approach was developed to sample and assess structures with dopings similar to the complexion. For this, the design of experiment Box–Behnken design[103] was used and the limits according to the doping relevant in the investigated areas were chosen. For the LSM-based design, a cubic LSM cell was chosen as a base, with 12 La, 12 Mn and 36 O. For the complexion designs, a cubic ZrO_2 containing 32 Zr and 64 O was chosen. Oxygen vacancies were chosen to be closest to a neutral cell and the oxygen charge of the force field adapted to reach full neutrality of the cells during relaxation. The resulting designs can be found in Table S5 (Supporting Information). Fifty cells were then randomly generated with the desired dopings and relaxed them with a force field that flexibly adjusts the oxygen charge in order to have charge-neutral cells. The similarity of the generated structures was assessed with the desired region in and around the complexion by comparing the dot product of the averaged elemental smooth overlap of atomic positions (SOAPs)[104] of the generated cells with the one in the complexion region. The complexion was split in three parts of 0.7 nm each, and chose furthermore to compute the a region of 0.7 nm which lies 0.7 nm in the direction of the LSM. Based on the Box–Behnken designs, the Non-dominated Sorting Genetic Algorithm (NSGA-II) of pymoo[105] was used to find dopings that can provide a chemical environment close to the structural template in the larger cells. For each of the proposed dopings, 50 random structures were generated. To assess the similarity to the larger cells, the chemical environment of the different structures was compared as described above. The resulting structures and their similarities can also be found in Figures S41, S42, S45, and S46 (Supporting Information), respectively. From the structure with the highest similarity, the one with the lowest potential energy was chosen to perform the EELS calculations.

EELS Simulation, DOS, and Projected DOS: The electronic structure code CASTEP[102] was used to calculate core excited states with the functional PBEsol+U with a Hubbard parameter of U = 5.0 eV for Mn. For ZrO_2-based cells containing up to 96 atoms, a k-grid of 2×2×2 was used. For $LaMnO_3$ based cells of up to 60 atoms, a 2×3×3 k-grid was used. Spectra and (p)DOS were obtained using OPTADOS[106] with an adaptive broadening (adaptive smearing = 0.4, core broadening = True, Gaussian width = 0.5, Lorentzian width = 0.1, Lorentzian scale = 0.2). The complexion and doped LSM spectra are averaged over all oxygen atoms in the

cell, meaning for each oxygen ion its own excited computation was performed. Full results of the pDOS calculation can be found in Figure S43 (Supporting Information).

Nudged Elastic Band (NEB): Nudged Elastic Band calculations were performed employing the force field. The simulation cell was cubic ZrO_2 containing 108 Zr and 216 O before doping and oxygen vacancy introduction. One Zr was always replaced by a La ion and a neighboring Zr removed to form a vacancy, in which the La diffuses during the simulation. For YSZ, 5 different random dopings were initialized by introducing 16 Y and 8 O vacancies.

Supporting Information

Supporting Information is available from the Wiley Online Library or from the author.

Acknowledgements

H.T. and X.Q.T. contributed equally to this work. The authors acknowledge in-depths discussion with Prof. Dr. Robert Schlögl and for granting access to the infrastructure of the AC department. This work was supported by the Deutsche Forschungsgemeinschaft (DFG, German Research Foundation) under the priority programme SPP 2080 DynaKat. H.T. gratefully acknowledges funding by the SPP 2080 "DynaKat" Early Career Research Scholarships for Female Scientists. T.G., F.P.S., and T.L. acknowledge support from the Federal Ministry of Education and Research (BMBF) in the framework of the project Catlab (03EW0015B). Moreover, this work was partially funded by the Deutsche Forschungsgemeinschaft (DFG, German Research Foundation) under Germany's Excellence Strategy– EXC2089/1–390776260. X.Q.T acknowledges the Deutsche Forschungsgemeinschaft (DFG) for funding this work in the framework of the Priority Program SPP 2080 "Catalysts and reactors under dynamic conditions for energy storage and conversion" under the grant number LU 2246/3-1. The authors thank the European Regional Development Fund and the State of Brandenburg for the Themis Z microscope (part of Potsdam Imaging and Spectral Analysis (PISA) facility). Additionally, X.Q.T. acknowledges Dr. T. Yamamoto (Kyushu University, Japan) for his support with the DigitalMicrograph script for drift-corrected STEM imaging. EDX-STEM measurements were performed on the JEM-ARM300F2 (JEOL) at Center for Electron Microscopy ZELMI, TU Berlin (Funded by the Deutsche Forschungsgemeinschaft (DFG, German Research Foundation) - Project 403371556). All computations were performed on the high-performance computer Raven of the Max Planck Computing & Data Facility.

Open access funding enabled and organized by Projekt DEAL.

Conflict of Interest

The authors declare no conflict of interest.

Data Availability Statement

The data that support the findings of this study are openly available at https://doi.org/10.17617/3.Q5KFFD.

Keywords

atomic resolution STEM, complexion, MIEC, molecular modeling, solid oxide cells

Received: November 27, 2024
Published online: December 31, 2024

[1] J. Luo, *Energy Storage Mater.* **2019**, *21*, 50.
[2] S. Stegmaier, R. Schierholz, I. Povstugar, J. Barthel, S. P. Rittmeyer, S. Yu, S. Wengert, S. Rostami, H. Kungl, K. Reuter, R. Eichel, C. Scheurer, *Adv. Energy Mater.* **2021**, *11*, 2100707.
[3] S. He, S. P. Jiang, *Prog. Nat. Sci.: Mater. Int.* **2021**, *31*, 341.
[4] S. P. Jiang, *Electrochem. Energy Rev.* **2022**, *5*, 21.
[5] A. Hauch, R. Küngas, P. Blennow, A. B. Hansen, J. B. Hansen, B. V. Mathiesen, M. B. Mogensen, *Science* **2020**, *370*, eaba6118.
[6] R. M. Ormerod, *Chem. Soc. Rev.* **2003**, *32*, 17.
[7] M. Sohal, J. O'Brien, C. Stoots, V. Sharma, B. Yildiz, A. Virkar, *J. Fuel Cell Sci. Technol.* **2012**, *9*, 1.
[8] S. E. Wolf, F. E. Winterhalder, V. Vibhu, L. G. J. B. De Haart, O. Guillon, R.-A. Eichel, N. H. Menzler, *J. Mater. Chem. A* **2023**, *11*, 17977.
[9] X. Yang, J. Hardy, C. A. Coyle, J. F. Bonnett, S. M. Mahserejian, J. W. Stevenson, *J. Electrochem. Soc.* **2022**, *169*, 024512.
[10] S. Zarabi Golkhatmi, M. I. Asghar, P. D. Lund, *Renew. Sust. Energ. Rev.* **2022**, *161*, 112339.
[11] Z. Pan, Q. Liu, Z. Yan, Z. Jiao, L. Bi, S. H. Chan, Z. Zhong, *Electrochem. Commun.* **2022**, *137*, 107267.
[12] R. Knibbe, M. L. Traulsen, A. Hauch, S. D. Ebbesen, M. Mogensen, *J. Electrochem. Soc.* **2010**, *157*, B1209.
[13] M. A. Laguna-Bercero, J. A. Kilner, S. J. Skinner, *Chem. Mater.* **2010**, *22*, 1134.
[14] J. T. Irvine, D. Neagu, M. C. Verbraeken, C. Chatzichristodoulou, C. Graves, M. B. Mogensen, *Nat. Energy* **2016**, *1*, 1.
[15] H.-J. Wang, M. R. De Guire, Z. Xing, G. Agnew, R. Goettler, Z. Liu, A. H. Heuer, *Metall. Mater. Trans. E* **2014**, *1*, 263.
[16] Y. Chen, Y. Fan, S. Lee, G. Hackett, H. Abernathy, K. Gerdes, X. Song, *J. Power Sources* **2019**, *438*, 227043.
[17] S. Lau, S. Singhal, *Proc. Corros* **1985**, *85*, 1.
[18] K. Yang, J.-H. Shen, K.-Y. Yang, I.-M. Hung, K.-Z. Fung, M.-C. Wang, *J. Power Sources* **2006**, *159*, 63.
[19] J. Labrincha, J. Frade, F. Marques, *J. Mater. Sci.* **1993**, *28*, 3809.
[20] A. Chen, J. Smith, K. Duncan, R. DeHoff, K. Jones, E. Wachsman, *J. Electrochem. Soc.* **2010**, *157*, B1624.
[21] D. Kim, A. Hunt, I. Waluyo, B. Yildiz, *J. Mater. Chem. A* **2023**, *11*, 7299.
[22] X. Liu, J. Che, H. Yi, J. Zhang, G. Liang, *J. Alloys Compd.* **2019**, *778*, 522.
[23] M. Keane, M. K. Mahapatra, A. Verma, P. Singh, *Int. J. Hydrog. Energy* **2012**, *37*, 16776.
[24] M. Ghamarinia, A. Babaei, C. Zamani, H. Aslannejad, *Chem. Eng. J. Adv.* **2023**, *15*, 100503.
[25] Q. Jeangros, M. Bugnet, T. Epicier, C. Frantz, S. Diethelm, D. Montinaro, E. Tyukalova, Y. Pivak, J. Van Herle, A. Hessler-Wyser, M. Duchamp, *Nat. Commun.* **2023**, *14*, 7959.
[26] M. S. Khan, X. Xu, R. Knibbe, Z. Zhu, *Renew. Sustain. Energy Rev.* **2021**, *143*, 110918.
[27] M. V. Ananyev, N. M. Porotnikova, V. A. Eremin, E. K. Kurumchin, *ACS Catal.* **2021**, *11*, 4247.
[28] F. Chiabrera, I. Garbayo, L. López-Conesa, G. Martín, A. Ruiz-Caridad, M. Walls, L. Ruiz-González, A. Kordatos, M. Núñez, A. Morata, S. Estradé, A. Chroneos, F. Peiró, A. Tarancón, *Adv. Mater.* **2019**, *31*, 1805360.
[29] S. He, K. Chen, M. Saunders, J. Li, C. Cui, S. P. Jiang, *J. Electrochem. Soc.* **2017**, *164*, F1437.
[30] S. He, K. Chen, M. Saunders, Z. Quadir, S. Tao, J. T. Irvine, C. Cui, S. P. Jiang, *Solid State Ion.* **2018**, *325*, 176.
[31] M. Backhaus-Ricoult, *Solid State Ion.* **2006**, *177*, 2195.
[32] M. Backhaus-Ricoult, K. Adib, T. S. Clair, B. Luerssen, L. Gregoratti, A. Barinov, *Solid State Ion.* **2008**, *179*, 891.
[33] S. J. Dillon, M. Tang, W. C. Carter, M. P. Harmer, *Acta Mater.* **2007**, *55*, 6208.

[34] P. R. Cantwell, M. Tang, S. J. Dillon, J. Luo, G. S. Rohrer, M. P. Harmer, *Acta Mater.* **2014**, *62*, 1.
[35] H. Türk, F.-P. Schmidt, T. Götsch, F. Girgsdies, A. Hammud, D. Ivanov, I. C. Vinke, L. de Haart, R.-A. Eichel, K. Reuter, R. Schlögl, A. Knop-Gericke, C. Scheurer, T. Lunkenbein, *Adv. Mater. Interfaces* **2021**, *8*, 2100967.
[36] H. Türk, T. Götsch, F.-P. Schmidt, A. Hammud, D. Ivanov, L. de Haart, I. C. Vinke, R.-A. Eichel, R. Schlögl, K. Reuter, A. Knop-Gericke, T. Lunkenbein, C. Scheurer, *ChemCatChem* **2022**, *14*, 202200300.
[37] T. Götsch, H. Tuerk, F.-P. Schmidt, I. C. Vinke, L. G. J. B. De Haart, R. Schlögl, K. Reuter, R.-A. Eichel, A. Knop-Gericke, C. Scheurer, T. Lunkenbein, *ECS Trans.* **2021**, *103*, 1331.
[38] S. W. Chee, T. Lunkenbein, R. Schlögl, B. Roldán Cuenya, *Chem. Rev.* **2023**, *123*, 13374.
[39] A. Hauch, S. H. Jensen, S. Ramousse, M. Mogensen, *J. Electrochem. Soc.* **2006**, *153*, A1741.
[40] Y. Tao, S. D. Ebbesen, M. B. Mogensen, *J. Power Sources* **2016**, *328*, 452.
[41] K. Chen, N. Ai, S. P. Jiang, *Int. J. Hydrog. Energy* **2012**, *37*, 10517.
[42] T. T. Fister, D. D. Fong, J. A. Eastman, P. M. Baldo, M. J. Highland, P. H. Fuoss, K. R. Balasubramaniam, J. C. Meador, P. A. Salvador, *Appl. Phys. Lett.* **2008**, *93*, 15.
[43] C. Graves, S. D. Ebbesen, S. H. Jensen, S. B. Simonsen, M. B. Mogensen, *Nat. Mater.* **2015**, *14*, 239.
[44] M. B. Mogensen, A. Hauch, X. Sun, M. Chen, Y. Tao, S. D. Ebbesen, K. V. Hansen, P. V. Hendriksen, *Fuel cells* **2017**, *17*, 434.
[45] M. P. Hoerlein, M. Riegraf, R. Costa, G. Schiller, K. A. Friedrich, *Electrochim. Acta* **2018**, *276*, 162.
[46] M. B. Mogensen, M. Chen, H. L. Frandsen, C. Graves, A. Hauch, P. V. Hendriksen, T. Jacobsen, S. H. Jensen, T. L. Skafte, X. Sun, *Fuel Cells* **2021**, *21*, 415.
[47] M. Yashima, S. Sasaki, M. Kakihana, Y. Yamaguchi, H. Arashi, M. Yoshimura, *Acta Crystallograph. Sect. B: Struct. Sci.* **1994**, *50*, 663.
[48] X. Wang, W. Huang, C. Zhu, Q. Chen, S. Pilla, G. Liang, *J. Mol. Liq.* **2018**, *265*, 31.
[49] B. Feng, T. Yokoi, A. Kumamoto, M. Yoshiya, Y. Ikuhara, N. Shibata, *Nat. Commun.* **2016**, *7*, 11079.
[50] R. Devanathan, W. J. Weber, S. C. Singhal, J. D. Gale, *Solid State Ionics* **2006**, *177*, 1251.
[51] M. O. Zacate, L. Minervini, D. J. Bradfield, R. W. Grimes, K. E. Sickafus, *Solid State Ionics* **2000**, *128*, 243.
[52] H.-J. Deiseroth, H. Müller-Buschbaum, *Z. Anorg. Allg. Chem.* **1970**, *375*, 152.
[53] Y. Wang, C. Cai, L. Li, L. Yang, Y. Zhou, G. Zhou, *AIP Adv.* **2016**, *6*, 095113.
[54] M. Subramanian, G. Aravamudan, G. S. Rao, *Prog. Solid State Chem.* **1983**, *15*, 55.
[55] N. Ishizawa, F. Marumo, S. Iwai, M. Kimura, T. Kawamura, *Acta Cryst. B* **1982**, *38*, 368.
[56] A. Mitterdorfer, L. Gauckler, *Solid State Ion.* **1998**, *111*, 185.
[57] M. Schubert, S. Senz, D. Hesse, *Solid State Ion.* **2008**, *179*, 453.
[58] Y.-L. Liu, K. Thydén, M. Chen, A. Hagen, *Solid State Ion.* **2012**, *206*, 97.
[59] B. Butz, P. Kruse, H. Störmer, D. Gerthsen, A. Müller, A. Weber, E. Ivers-Tiffée, *Solid State Ion.* **2006**, *177*, 3275.
[60] S. Chen, Y. Chen, H. Finklea, X. Song, G. Hackett, K. Gerdes, *Solid State Ion.* **2012**, *206*, 104.
[61] J. Salmon, Z. Harmany, C.-A. Deledalle, R. Willett, *J. Math. Imaging Vis.* **2014**, *48*, 279.
[62] T. Kawada, N. Sakai, H. Yokokawa, M. Dokiya, *Solid State Ion.* **1992**, *53*, 418.
[63] J. Sunarso, S. Baumann, J. Serra, W. Meulenberg, S. Liu, Y. Lin, J. D. Da Costa, *J. Membr. Sci.* **2008**, *320*, 13.
[64] S. P. Jiang, *Int. J. Hydrog. Energy* **2019**, *44*, 7448.
[65] R. Knibbe, A. Hauch, J. Hjelm, S. D. Ebbesen, M. Mogensen, *Green* **2011**, *1*, 141.
[66] K. Chen, S. P. Jiang, *Int. J. Hydrog. Energy* **2011**, *36*, 10541.
[67] S. R. Foit, I. C. Vinke, L. G. J. D. Haart, R. Eichel, *Angew. Chem. Int. Ed.* **2017**, *56*, 5488.
[68] J. Kim, H.-I. Ji, H. P. Dasari, D. Shin, H. Song, J.-H. Lee, B.-K. Kim, H.-J. Je, H.-W. Lee, K. J. Yoon, *Int. J. Hydrog. Energy* **2013**, *38*, 1225.
[69] F. Tietz, D. Sebold, A. Brisse, J. Schefold, *J. Power Sources* **2013**, *223*, 129.
[70] A. Chen, J. R. Smith, K. L. Duncan, R. T. DeHoff, K. S. Jones, E. D. Wachsman, *J. Electrochem. Soc.* **2010**, *157*, B1624.
[71] Z. Pan, Q. Liu, M. Ni, R. Lyu, P. Li, S. H. Chan, *Int. J. Hydrog. Energy* **2018**, *43*, 5437.
[72] K. Chen, S. P. Jiang, *Int. J. Hydrog. Energy* **2011**, *36*, 10541.
[73] S. P. Jiang, J. G. Love, *Solid State Ion.* **2001**, *138*, 183.
[74] N. Caillol, M. Pijolat, E. Siebert, *Appl. Surf. Sci.* **2007**, *253*, 4641.
[75] A. K. Huber, M. Falk, M. Rohnke, B. Luerssen, M. Amati, L. Gregoratti, D. Hesse, J. Janek, *J. Catal.* **2012**, *294*, 79.
[76] D. Kim, R. Bliem, F. Hess, J.-J. Gallet, B. Yildiz, *J. Am. Chem. Soc.* **2020**, *142*, 3548.
[77] N. Li, M. Keane, M. K. Mahapatra, P. Singh, *Int. J. Hydrog. Energy* **2013**, *38*, 6298.
[78] J. Li, X. Zhou, C. Wu, L. Zhao, B. Dong, S. Wang, B. Chi, *Chem. Eng. J.* **2022**, *438*, 135446.
[79] J. Laurencin, M. Hubert, D. F. Sanchez, S. Pylypko, M. Morales, A. Morata, B. Morel, D. Montinaro, F. Lefebvre-Joud, E. Siebert, *Electrochim. acta* **2017**, *241*, 459.
[80] A. Nechache, A. Mansuy, M. Petitjean, J. Mougin, F. Mauvy, B. A. Boukamp, M. Cassir, A. Ringuedé, *Electrochim. acta* **2016**, *210*, 596.
[81] D. Wang, J. Yang, J. Liu, X. Li, R. Li, M. Cai, T.-K. Sham, X. Sun, *J. Mater. Chem. A* **2014**, *2*, 2306.
[82] X. Li, J. Liu, M. N. Banis, A. Lushington, R. Li, M. Cai, X. Sun, *Energy Environ. Sci.* **2014**, *7*, 768.
[83] L. Han, C.-T. Hsieh, B. Chandra Mallick, J. Li, Y. Ashraf Gandomi, *Nanoscale Adv.* **2021**, *3*, 2728.
[84] S. P. Jiang, *Mater. Sci. Eng. A* **2006**, *418*, 199.
[85] A. Ovalle, J. Ruizmorales, J. Canalesvazquez, D. Marrerolopez, J. Irvine, *Solid State Ion.* **2006**, *177*, 1997.
[86] J. Li, T. Lv, N. Hou, P. Li, X. Yao, L. Fan, T. Gan, Y. Zhao, Y. Li, *Int. J. Hydrog. Energy* **2017**, *42*, 22294.
[87] F. Yang, H. Zhang, L. Li, I. M. Reaney, D. C. Sinclair, *Chem. Mater.* **2016**, *28*, 5269.
[88] A. Leonide, V. Sonn, A. Weber, E. Ivers-Tiffée, *J. Electrochem. Soc.* **2007**, *155*, B36.
[89] K. Zhang, D. Zhang, Y. Wang, Y. Li, C. Ren, M. Ding, T. Liu, *Nano Res.* **2023**, *16*, 10992.
[90] D. Zhang, Y. Wang, Y. Peng, Y. Luo, T. Liu, W. He, F. Chen, M. Ding, *Adv. Powder Mater.* **2023**, *2*, 100129.
[91] E. Okunishi, I. Ishikawa, H. Sawada, F. Hosokawa, M. Hori, Y. Kondo, *Microsc. Microanal.* **2009**, *15*, 164.
[92] T. Lunkenbein, F. Girgsdies, A. Wernbacher, J. Noack, G. Auffermann, A. Yasuhara, A. Klein-Hoffmann, W. Ueda, M. Eichelbaum, A. Trunschke, R. Schlögl, M. G. Willinger, *Angew. Chem.* **2015**, *127*, 6932.
[93] R. Ishikawa, E. Okunishi, H. Sawada, Y. Kondo, F. Hosokawa, E. Abe, *Nat. Mater.* **2011**, *10*, 278.
[94] L. Jones, A. Varambhia, H. Sawada, P. Nellist, *J. Microsc.* **2018**, *270*, 176.
[95] S. Hillyard, J. Silcox, *Ultramicroscopy* **1995**, *58*, 6.
[96] D. A. Muller, N. Nakagawa, A. Ohtomo, J. L. Grazul, H. Y. Hwang, *Nature* **2004**, *430*, 657.
[97] Z. Ji, M. Hu, H. L. Xin, *Sci. Rep.* **2023**, *13*, 14132.
[98] J. Barthel, *Ultramicroscopy* **2018**, *193*, 1.

[99] Y. Seto, M. Ohtsuka, *J. Appl. Crystallogr.* **2022**, *55*, 397.
[100] H. W. Brinkman, *Chem. Phys. Lett.* **1995**, *247*, 386.
[101] M. S. Islam, M. Cherry, C. R. A. Catlow, *J. Solid State Chem.* **1996**, *124*, 230.
[102] S. J. Clark, M. D. Segall, C. J. Pickard, P. J. Hasnip, M. I. Probert, K. Refson, M. C. Payne, *Z. Kristallog.* **2005**, *220*, 567.
[103] G. E. P. Box, S. Hunter, W. G. Hunter, *Statistics for Experimenters*, Wiley, New York, NY, USA **1978**.
[104] A. P. Bartók, R. Kondor, G. Csányi, *Phys, Rev. B Condens. Matter* **2013**, *87*, 1.
[105] J. Blank, K. Deb, *IEEE Access* **2020**, *8*, 89497.
[106] R. J. Nicholls, A. J. Morris, C. J. Pickard, J. R. Yates, *J. Phys. Conf. Ser* **2012**, *371*, 2.